Journal of Pathology
J Pathol September 2023; **261**: 28–42
Published online 22 June 2023 in Wiley Online Library
(wileyonlinelibrary.com) DOI: 10.1002/path.6144

ORIGINAL ARTICLE

ELF3 suppresses gallbladder cancer development through downregulation of the EREG/EGFR/mTOR complex 1 signalling pathway

Takeharu Nakamura[1], Yoshihiro Nishikawa[1,2*], Masahiro Shiokawa[1*], Haruhiko Takeda[1], Masataka Yokode[1], Shimpei Matsumoto[1], Yuya Muramoto[1], Sakiko Ota[1], Hiroyuki Yoshida[1], Hirokazu Okada[1], Takeshi Kuwada[1], Saiko Marui[1], Tomoaki Matsumori[1], Takahisa Maruno[1], Norimitsu Uza[1], Yuzo Kodama[2], Etsuro Hatano[3] and Hiroshi Seno[1]

[1] *Department of Gastroenterology and Hepatology, Kyoto University Graduate School of Medicine, Kyoto, Japan*
[2] *Department of Gastroenterology, Kobe University Graduate School of Medicine, Kobe, Japan*
[3] *Division of Hepato-Biliary-Pancreatic Surgery and Transplantation, Department of Surgery, Kyoto University Graduate School of Medicine, Kyoto, Japan*

**Correspondence to: Y Nishikawa or M Shiokawa, Department of Gastroenterology and Hepatology, Kyoto University Graduate School of Medicine, 54 Shogoin-Kawahara-cho, Sakyo-ku, Kyoto, 606-8507, Japan. E-mail: nishi328@kuhp.kyoto-u.ac.jp (Y Nishikawa) or E-mail: machan@kuhp.kyoto-u.ac.jp (M Shiokawa).*

Abstract

The prognosis of gallbladder cancer (GBC) remains poor, and a better understanding of GBC molecular mechanisms is important. Genome sequencing of human GBC has demonstrated that loss-of-function mutations of E74-like ETS transcription factor 3 (*ELF3*) are frequently observed, with ELF3 considered to be a tumour suppressor in GBC. To clarify the underlying molecular mechanisms by which ELF3 suppresses GBC development, we performed *in vivo* analysis using a combination of autochthonous and allograft mouse models. We first evaluated the clinical significance of ELF3 expression in human GBC tissues and found that low ELF3 expression was associated with advanced clinical stage and deep tumour invasion. For *in vivo* analysis, we generated *Pdx1-Cre*; *Kras*^{G12D}; *Trp53*^{R172H}; *Elf3*$^{f/f}$ (KPCE) mice and *Pdx1-Cre*; *Kras*^{G12D}; *Trp53*^{R172H}; *Elf3*$^{wt/wt}$ (KPC) mice as a control and analysed their gallbladders histologically. KPCE mice developed larger papillary lesions in the gallbladder than those developed by KPC mice. Organoids established from the gallbladders of KPCE and KPC mice were analysed *in vitro*. RNA sequencing showed upregulated expression of epiregulin (*Ereg*) in KPCE organoids, and western blotting revealed that EGFR/mechanical targets of rapamycin complex 1 (mTORC1) were upregulated in KPCE organoids. In addition, ChIP assays on *Elf3*-overexpressing KPCE organoids showed that ELF3 directly regulated *Ereg*. *Ereg* deletion in KPCE organoids (using CRISPR/Cas9) induced EGFR/mTORC1 downregulation, indicating that ELF3 controlled EGFR/mTORC1 activity through regulation of *Ereg* expression. We also generated allograft mouse models using KPCE and KPC organoids and found that KPCE organoid allograft tumours exhibited poorly differentiated structures with mTORC1 upregulation and mesenchymal phenotype, which were suppressed by *Ereg* deletion. Furthermore, EGFR/mTORC1 inhibition suppressed cell proliferation and epithelial–mesenchymal transition in KPCE organoids. Our results suggest that ELF3 suppresses GBC development via downregulation of EREG/EGFR/mTORC1 signalling. EGFR/mTORC1 inhibition is a potential therapeutic option for GBC with *ELF3* mutation.

Keywords: ELF3; gallbladder cancer; EREG; EGFR; mTOR complex 1

Received 24 January 2023; Revised 1 May 2023; Accepted 16 May 2023

No conflicts of interest were declared.

Introduction

Gallbladder cancer (GBC) is the most common type of biliary tract cancer (BTC) with high lethality [1]. Its poor prognosis is partially attributed to the anatomical characteristics of the gallbladder. Lack of both submucosal and serosal layers on the hepatic side of gallbladder facilitates tumour invasion and metastasis, which is associated with diagnosis at an advanced stage [2]. Lack of adequately effective therapies remains a major cause of poor prognosis of GBC. Although several efforts have been made to establish effective therapies, the 5-year survival rate of GBC remains under 30% [3]. To improve the prognosis, understanding the molecular mechanisms underlying GBC formation and identifying new therapeutic targets are important.

Several studies on genome sequencing of BTC, including GBC, recently revealed that many significantly altered

genes were included in the erb-b2 receptor tyrosine kinase (ERBB) pathway [4–6]. The ERBB family comprises four receptor tyrosine kinases: EGFR/ERBB1, ERBB2, ERBB3, and ERBB4 [7,8]. Activated ERBB stimulates various downstream pathways, such as the RAS/MAPK and PI3K/AKT pathways, which are involved in the development of many types of human cancers [7–10]. GBCs that harbour gene mutations in the ERBB pathway are associated with worse prognosis; therefore, the ERBB pathway is an important factor in GBC development [4].

Integrated genomic analysis of human GBC revealed that E74-like ETS transcription factor 3 (*ELF3*) is the second most frequently mutated gene and is altered in up to 20% of samples [6]. Other genome sequencing analyses also demonstrated that *ELF3* was highly mutated in extrahepatic cholangiocarcinoma and ampullary carcinoma [5,11]. ELF3 is an epithelium-specific transcription factor belonging to the ETS transcription family and is involved in various physiological functions, such as cell differentiation/proliferation, cell cycle adjustment, apoptosis, and angiogenesis, in normal tissues [12]. In cancers, various malignancies harbour *ELF3* alterations [13]. ELF3 plays an important role in cancer development; however, whether ELF3 functions as a tumour suppressor or promoter depends on the primary organ [13–20]. In BTCs, including GBC, most *ELF3* mutations are the loss-of-function type, such as frameshifts and stop gains [5,6,11]. Moreover, xenografts of *ELF3*-overexpressing human BTC cells showed a better-differentiated tubular structure than that seen in control cells [21]. Thus, ELF3 is considered a suppressor of tumour development and epithelial–mesenchymal transition (EMT) in BTC; however, the molecular mechanism by which ELF3 suppress BTC development and EMT has not been fully elucidated.

In this study, we show that ELF3 plays a tumour-suppressive role in GBC development in mice. ELF3 negatively regulates mRNA expression of *Ereg*, the gene-encoding ligand of ERBB receptors, and consequently suppresses EGFR/mTOR complex 1 (mTORC1) activity.

Materials and methods

Study approval

This study was conducted in compliance with the Helsinki Declaration and the Ethical Guidelines for Medical and Health Research Involving Human Subjects. The protocol was approved by the Human Ethics Review Committee of Kyoto University Hospital (Approval No. G616). Informed consent was obtained from all patients with an opt-out method. All experiments with mice were approved by the Ethics Committee for Animal Experiments and performed in accordance with the guidelines of the Animal Experiments of Kyoto University (Approval No. 22581).

Patients

GBC specimens were obtained from surgically resected or liver biopsy tissues of 85 consecutive patients admitted to Kyoto University Hospital (Kyoto, Japan) between November 2004 and October 2020. Patient medical records were reviewed from their first visit to our institute until November 2021, loss to follow-up, or death. The detailed clinical information of patients with GBC is shown in supplementary material, Table S1.

Mice

Pdx1-Cre [22], *LSL-Kras*^{G12D} [23], and *LSL-Trp53*^{R172H} mice [24] were established as described previously. *Elf3* flox mice (C57BL/6N-Elf3$^{tm1a(KOMP)Wtsi}$, RRID: MMRRC_047524-UCD) were purchased from UC Davis KOMP Repository (Davis, CA, USA) and crossed with *B6-Tg* (*CAG-FLPe*)*36* mice to delete the inserted cassette floxed by the FRT site. NOD.CB17-*Prkdc*^{scid}/Jcl mice were purchased from CLEA Japan (Tokyo, Japan). All mice were maintained in a specific-pathogen-free facility at the Kyoto University Faculty of Medicine (Kyoto, Japan) with food and water provided *ad libitum*. Mice were housed at two to six per cage irrespective of their genotype and used without distinction of sex. For the gallbladder histological analysis, 9 or 10 mice per group were sacrificed after fasting for 2 h. For 5-bromo-4-chloro-3-indolyl-β-D-galactoside (X-gal, Wako, Osaka, Japan) staining of the biliary tract, three *Pdx1-Cre*; *Rosa26*$^{LSL\text{-}LacZ}$ mice were used. For organoid establishment, three or four mice were used in each organoid group.

Semiquantification of immunostaining intensity in human GBC samples

For the semiquantification of immunostaining intensity in human GBC samples, the dominant immunostaining intensity was determined on a scale of 0 to 3: 0 = negative, 1 = weak, 2 = moderate, 3 = strong. For ELF3 semiquantification, moderate intensity was defined as one similar to that of normal gallbladder epithelial cells, and low and high expression of ELF3 were defined as staining intensities of 0–1 and 2–3, respectively. Scoring was performed by two investigators.

Statistical analysis

Data are presented as the mean ± SEM. Statistical comparisons between groups were performed using Student's *t*-test, paired *t*-test, or one-way ANOVA test. $P < 0.05$ was considered statistically significant. All statistical analyses were performed using either GraphPad Prism 9 (GraphPad, San Diego, CA, USA, RRID:SCR_002798) or R version 4.0.3. Overall survival (OS) was defined as the interval from the date of diagnosis to the date of death or censoring for any cause and estimated using the Kaplan–Meier method. The difference between the two groups was calculated using the Gehan–Breslow–Wilcoxon test. Hazard ratios were

calculated using Cox proportional hazards regression analysis (Mantel–Haenszel method).

Further descriptions of allograft mouse models, histology, organoids and cell lines, lentivirus transfection, RNA isolation and RNA sequencing (RNA-seq), western blot analyses, RT-qPCR, ChIP, cell proliferation assays, scratch assays, invasion assays, and analysis of human GBC RNA-seq data can be found in Supplementary materials and methods. The antibodies and primer sets used in this study are listed in supplementary material, Tables S2 and S3, respectively.

Results

Low ELF3 expression in GBC is associated with advanced clinical stage and deep invasion of tumours

To elucidate ELF3 expression in epithelial cells of gallbladder and other parts of the extrahepatic biliary tract (EHBT) in humans, we performed immunohistochemistry (IHC) on normal human tissues. ELF3 was expressed in the epithelial cells of the EHBT, including the gallbladder, extrahepatic bile duct (EHBD), and papilla of Vater (Figure 1A). We also examined tissues from patients with chronic cholecystitis and precancerous lesions of the EHBT and revealed that ELF3 was also expressed in the epithelial cells of these tissues (Figure 1A).

Next, to evaluate ELF3 expression in GBC tissues, we performed IHC on GBC tissues obtained from GBC patients and semiquantitatively evaluated staining intensity (supplementary material, Table S1). Low ELF3 expression was observed in more than half of all samples (Figure 1B). We further investigated the clinical significance of ELF3 expression by comparing the clinical characteristics of the low- and high-ELF3-expression groups. Notably, low ELF3 expression was associated with advanced clinical stage and deep tumour invasion (Table 1). The Kaplan–Meier method and Gehan–Breslow–Wilcoxon test demonstrated that the OS of the low-ELF3-expression group (median: 672 days) tended to be shorter than that of the high-ELF3-expression group (median: 1,713 days; Figure 1C). These results suggest that ELF3 plays a tumour-suppressive role in human GBC, especially in terms of tumour invasiveness.

ELF3 is not essential for the development and maintenance of the EHBT in mice

Pdx1 is expressed in embryonic extrahepatic biliary epithelial cells [25], and Cre recombinase expression driven by the *Pdx1* promoter in extrahepatic biliary epithelial cells was confirmed using X-gal staining on the EHBT of adult *Pdx1-Cre*; *Rosa26*$^{LSL\text{-}LacZ}$ mice (supplementary material, Figure S1). Therefore, we generated *Pdx1-Cre*; *Elf3*$^{f/f}$ mice to investigate the functional role of ELF3 in EHBT development (supplementary material, Figure S2A). The EHBT of *Pdx1-Cre*; *Elf3*$^{f/f}$ mice showed no obvious changes in gross appearance or histological abnormalities compared with that of control *Pdx1-Cre*; *Elf3*$^{wt/wt}$ mice (supplementary material, Figure S2B,C). IHC for ELF3 revealed that, similar to that in human tissues, ELF3 was expressed in extrahepatic biliary epithelial cells of control mice and confirmed that *Elf3* was efficiently deleted in the extrahepatic biliary epithelial cells in *Pdx1-Cre*; *Elf3*$^{f/f}$ mice (supplementary material, Figure S2C).

To investigate the role of ELF3 in EHBT homeostasis, we evaluated these mice at 1 year of age. The EHBT of *Pdx1-Cre*; *Elf3*$^{f/f}$ mice showed no changes in gross appearance or histological abnormalities compared with that of control mice, and IHC for ELF3 showed that *Elf3*-deleted extrahepatic biliary cells were maintained in *Pdx1-Cre*; *Elf3*$^{f/f}$ mice (supplementary material, Figure S2D). These data suggest that ELF3 is not essential for EHBT development and homeostasis in mice.

Elf3 deletion accelerates tumourigenesis in the gallbladder in the context of *Kras* and *Trp53* mutation in mice

TP53 is the most frequently mutated gene and is found altered in half of human GBC cases [4,6]. Therefore, we generated *Pdx1-Cre*; *Trp53*^{R172H}; *Elf3*$^{f/f}$ (PCE) mice and *Pdx1-Cre*; *Trp53*^{R172H}; *Elf3*$^{wt/wt}$ (PC) mice as controls to evaluate whether *Elf3* deletion and *Trp53* mutation cause tumourigenesis in the gallbladder (supplementary material, Figure S3A). Although the supranuclear mucinous change in gallbladder epithelial cells in PCE mice at 40–45 weeks of age was slightly more prominent than that in PC mice, neither PCE nor PC mice showed obvious tumour formation in the EHBT (supplementary material, Figure S3B,C). This indicates that *Trp53* inactivation is not sufficient to cause tumour formation in the gallbladder of mice, regardless of the presence or absence of *Elf3*, and additional oncogenic driver mutations are essential.

In human GBC, several substantially altered genes have been identified in the ERBB/RAS/PI3K pathway, including *KRAS* [4,6], and oncogenic *Kras*^{G12D} mutations have been reported to induce gallbladder adenomas in mice [26]. Therefore, we generated *Pdx1-Cre*; *Kras*^{G12D}; *Trp53*^{R172H}; *Elf3*$^{f/f}$ (KPCE) mice and *Pdx1-Cre*; *Kras*^{G12D}; *Trp53*^{R172H}; *Elf3*$^{wt/wt}$ (KPC) control mice (Figure 2A). While KPC mice are widely accepted models of pancreatic ductal cancer [27], we used them to investigate the impact of *Elf3* deletion on *Kras* activation and *Trp53* inactivation in the gallbladder epithelium. At 16–18 weeks of age, the gallbladder wall of KPCE mice was thicker than that of KPC mice (Figure 2B). Histologically, massive papillary lesions were observed in KPCE mice, whereas papillary lesions in KPC mice were relatively thin (Figure 2C). The occupancy rate of papillary lesions in the gallbladder lumen was significantly higher in KPCE mice than in KPC mice (Figure 2D). Furthermore, the epithelial cells in KPCE mice showed a higher grade of cellular atypia

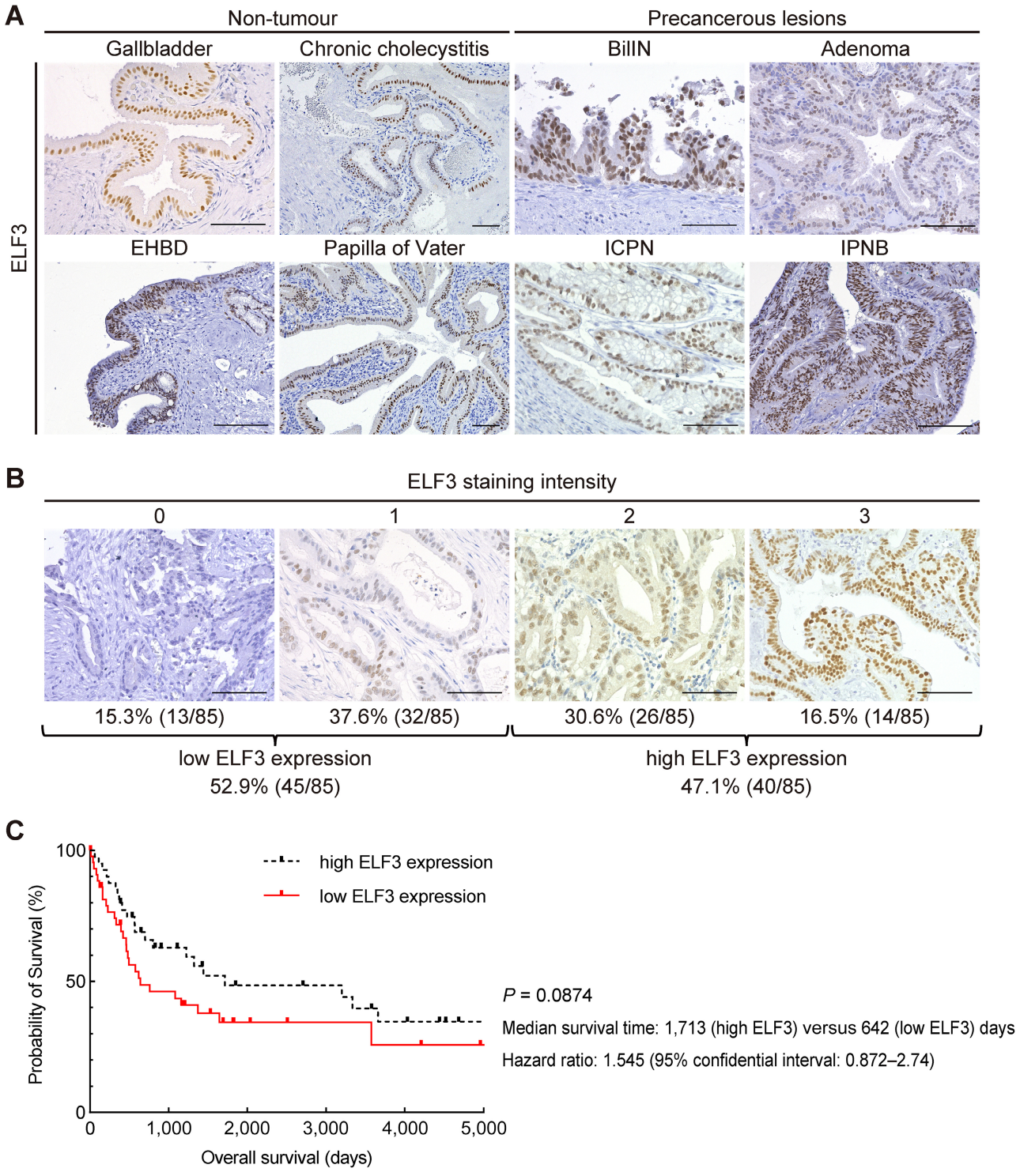

Figure 1. ELF3 expression of human EHBT tissues. (A) Representative immunostaining for ELF3 in non-tumour tissues (left) and precancerous lesion tissues (right) of human EHBT. Non-tumour tissues include normal gallbladder, EHBD, papilla of Vater, and chronic cholecystitis. Precancerous lesions include biliary intraepithelial neoplasia (BilIN), adenoma, intracystic papillary neoplasm (ICPN), and intraductal papillary neoplasm of bile duct (IPNB). Scale bars, 100 μm. (B) Representative immunostaining for ELF3 in human gallbladder cancer and scaling of dominant staining intensity. Scale bars, 100 μm. (C) Kaplan–Meier curves of overall survival of low and high ELF3 expression groups ($n = 45$ and 40, respectively). $P = 0.0874$, Gehan–Breslow–Wilcoxon test. See also Table 1 and supplementary material, Table S1, for clinical information of GBC patients and differences between the two groups.

than those in KPC mice and exhibited pleomorphic nuclei with anisonucleosis and distinct nucleoli, whereas those in KPC mice showed almost no atypical change (Figure 2C). These results indicate that *Elf3* deletion accelerates tumourigenesis in the gallbladder in the context of *Kras* and *Trp53* mutations in mice.

Table 1. Association between histological ELF3 expression and clinicopathological characteristics in GBC patients.

	Low ELF3 expression ($n = 45$)	High ELF3 expression ($n = 40$)	*P* value
Sex, male/female, *n*	25/20	15/25	0.128
Median age (range), years	70 (44–88)	73 (49–85)	0.142
Clinical stage (UICC 8th), *n*			
0/I/II/III/IVA/IVB	6/2/7/14/2/14	4/6/14/5/0/11	
0, I, II versus III, IVA, IVB	15/30	24/16	0.0172*
T stage, (UICC 8th), *n*			
Tis/T1/T2/T3/T4	6/2/9/23/5	4/6/17/8/5	
Tis, T1, T2 versus T3, T4	17/28	27/13	0.00895**
N stage (UICC 8th), *n*			
N0/N1/N2	23/21/1	28/11/1	0.125
M stage (UICC 8th), *n*			
M0/M1	31/14	29/11	0.813
Main histological type, *n*			
pap, tub1/tub2-3, por, undiff/others	17/19/6	22/14/4	0.498
Initial treatment, *n*			
Surgery/Chemotherapy/BSC	40/4/1	33/7/0	0.335
Recurrence after resection, *n*			
Yes/no	20/20	10/23	0.101

BSC, best supportive care; UICC, Union for International Cancer Control.
*$p < 0.05$;
**$p < 0.01$, Student's *t*-test.

ERBB signalling pathway is upregulated in KPCE organoids and ELF3 directly downregulates *Ereg* and *Areg* expression

We further investigated the mechanism underlying tumour formation in the gallbladders of KPCE mice before the development of papillary lesions using organoids generated from the gallbladder epithelium of KPC and KPCE mice at 10–11 weeks of age (Figure 3A). A previous report revealed that EGF and FGF removal from the culture medium could efficiently select tumour organoids harbouring *KRAS* mutation [28], and thus we used serum-free culture medium without EGF or FGF for organoid culture and confirmed the recombination of $Kras^{G12D}$ and $Trp53^{R172H}$ alleles and efficient selection of organoids (supplementary material, Figure S4A). In addition, to verify that these organoids were derived from gallbladder epithelial cells, we also established organoids from the common bile duct of the same mice and evaluated mRNA expression of the gallbladder and common bile duct organoids using RT-qPCR (supplementary material, Figure S4B). RT-qPCR revealed that the gallbladder-derived organoids had higher levels of the gallbladder-specific marker *Sox17* and lower levels of the common bile duct-specific markers *Slc28a3* and *Kcne3* compared to those in the common bile duct organoids (supplementary material, Figure S4C) [29], indicating that the gallbladder organoids could be established without contamination by epithelial cells from other regions of the bile duct.

To investigate the underlying transcript changes in the gallbladders of KPCE mice before the development of papillary lesions, RNA-seq was performed on the gallbladder organoids (Figure 3B). Gene set enrichment analysis (GSEA) demonstrated that the ERBB signalling pathway was significantly enriched in KPCE organoids compared to that in KPC organoids (Figure 3C). In addition, EMT-related genes tended to be enriched in KPCE organoids (Figure 3C). Kyoto Encyclopaedia of Genes and Genomes pathway analysis also revealed that the ERBB signalling pathway and the downstream PI3K/AKT and MAPK signalling pathways were significantly enriched in KPCE organoids (Figure 3D). Among the differentially expressed genes (DEGs) in the ERBB signalling pathway in KPCE organoids, we focused on *Ereg* and *Areg* (Figure 3E). Ereg and Areg encode epiregulin (EREG) and amphiregulin (AREG), respectively, which are members of the EGF family of proteins and ligands of the ERBB receptors. EREG and AREG can upregulate ERBB downstream PI3K/AKT/mTORC1 and RAS/MAPK pathways and are involved in cancer progression [8,30,31]. Based on these findings, we hypothesised that ELF3 downregulates *Ereg* and *Areg* expression and consequently suppresses the downstream signalling pathway of ERBB receptors.

To test this hypothesis, we generated *Elf3*-overexpressing KPCE (KPCE-*Elf3* OE) organoids. RT-qPCR analysis confirmed that *Elf3* mRNA levels were increased and *Ereg* mRNA levels were significantly decreased in KPCE-*Elf3* OE organoids compared with those in KPCE organoids (Figure 3F). *Areg* mRNA levels tended to be lower in KPCE-*Elf3* OE organoids than in KPCE organoids, though not significantly (Figure 3F). Furthermore, ChIP assays performed on KPCE-*Elf3* OE organoids clarified that ELF3 directly bound to *Ereg* and *Areg* promoter regions (Figure 3G). These results indicate that ELF3 directly downregulates *Ereg* and *Areg* mRNA expression.

EGFR/mTORC1 signal and EMT are upregulated in KPCE gallbladder tumours

To further study the ERBB downstream signalling pathways, we generated organoids from the gallbladder of KPC and KPCE mice at 16–18 weeks of age and performed several analyses on these organoids (Figure 4A). RT-qPCR analysis revealed decreased *Cdh1* expression and increased expression of *Snai1* and *Cd133* in KPCE organoids, indicating that dedifferentiation and EMT were induced in KPCE organoids (Figure 4B). We next evaluated their proliferation abilities. Consistent with the result of histological analysis on mouse models, KPCE organoids showed a tendency toward higher proliferation than KPC organoids in proliferation assays (Figure 4C). We also evaluated the protein expression levels of the pathways using western blotting of proteins from these organoids. Interestingly, the phosphorylated EGFR (p-EGFR) level was increased in KPCE organoids (Figure 4D). Ribosomal protein S6 (RPS6) kinase (RPS6K) and eukaryotic translation initiation factor 4E-binding protein 1 (4E-BP1), the main downstream targets of mTORC1, were also highly phosphorylated in KPCE organoids (Figure 4D). Additionally, the expression of the

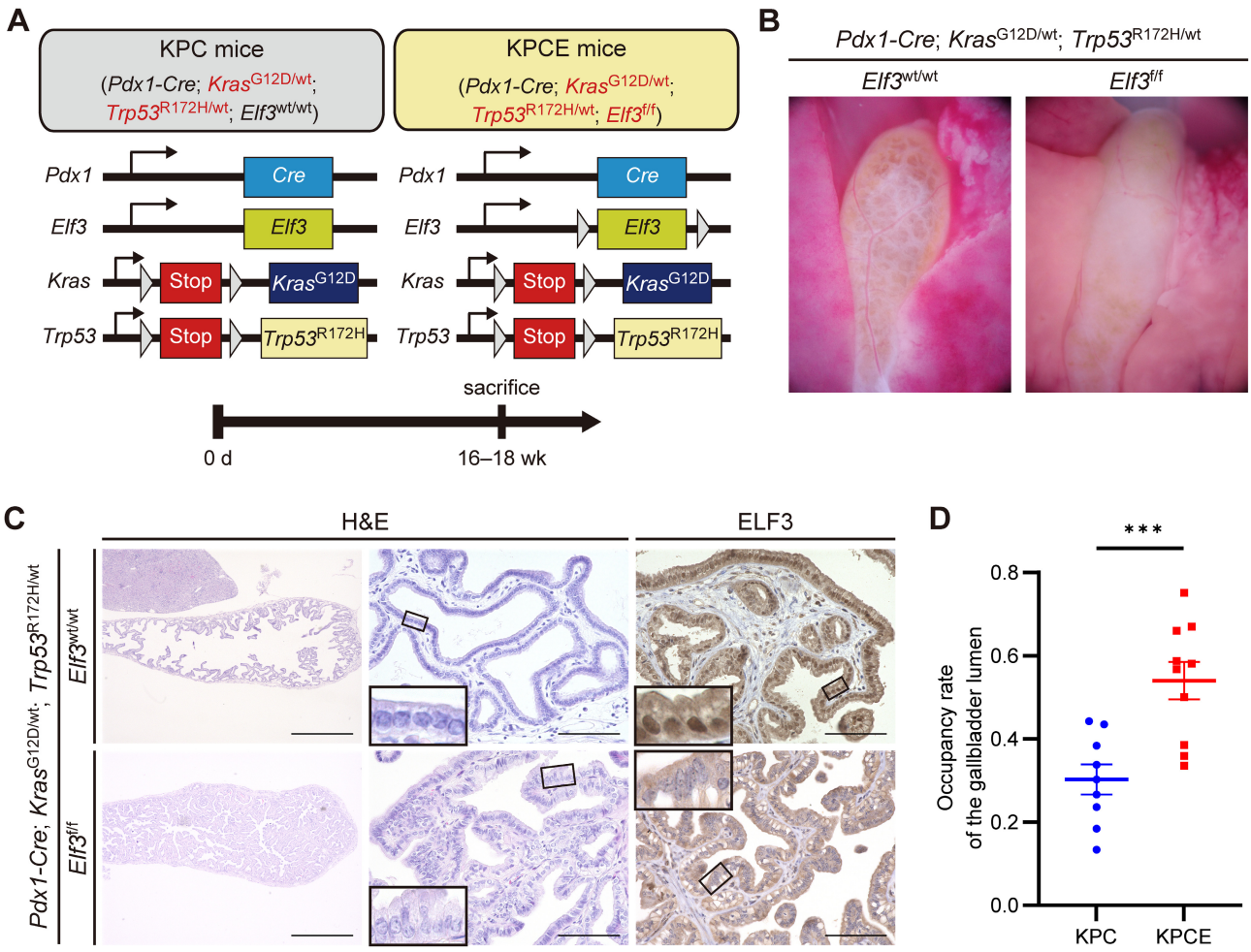

Figure 2. *Elf3* deletion accelerates tumourigenesis in gallbladder in context of *Kras* and *Trp53* mutation in mice. (A) Genetic designs of KPC (*Pdx1-Cre*; $Kras^{G12D/wt}$; $Trp53^{R172H/wt}$; $Elf3^{wt/wt}$) and KPCE (*Pdx1-Cre*; $Kras^{G12D/wt}$; $Trp53^{R172H/wt}$; $Elf3^{f/f}$) mice. Arrowheads indicate loxP sites. Cre-mediated deletion induces monoallelic mutation of *Kras* and *Trp53* and biallelic deletion of *Elf3*. (B) Gross appearance of gallbladder of KPC and KPCE mice at 16–18 weeks of age. (C) H&E staining and immunostaining for ELF3 in gallbladder tissues of KPC and KPCE mice at 16–18 weeks of age. Insets show higher-magnification images. Scale bars (left pictures), 1 mm; (middle and right pictures), 100 μm. (D) Quantification of papillary lesion occupancy rates in gallbladder lumen of KPC and KPCE mice ($n = 9$ and 10, respectively). $^{***}P < 0.01$, Student's *t*-test. Occupancy rate was calculated as follows: 1 –inner-gallbladder cavity area/area enclosed by outermost layer of gallbladder wall.

mesenchymal marker proteins, N-cadherin, ZEB1, and SNAI1, was higher in the KPCE than KPC organoids (Figure 4D). To validate these results in mouse models, we performed IHC on KPC and KPCE mice. Notably, EREG, p-EGFR, phosphorylated RPS6 (p-RPS6), and phosphorylated 4E-BP1 (p-4E-BP1) were highly expressed in KPCE gallbladder (Figure 4E). These findings suggest that EREG and p-EGFR expression are increased by *Elf3* deletion, which leads to mTORC1 upregulation and EMT in murine gallbladder organoids.

We further analysed the signalling pathways between EGFR and mTORC1. The PI3K/AKT and RAS/MAPK signalling pathways, which are main targets of ERBB downstream signalling, activate mTORC1 [32]. In addition, AMP-activated protein kinase (AMPK) also modulates mTORC1 activity. AMPK is activated by intracellular ATP/AMP level, low glucose level, hypoxia, ischemia, and heat shock, and then suppresses mTORC1 [32,33]. Western blotting revealed that phosphorylated PI3K and AKT levels were increased, while the phosphorylated AMPK level was decreased in KPCE organoids (Figure 4D). These findings indicate that mTORC1 in KPCE organoids is modulated by several signalling cascades, including PI3K/AKT and AMPK. To validate this suggestion, we evaluated PI3K/AKT, AMPK, and mTORC1 activity in KPCE organoids following administration of an EGFR inhibitor, afatinib. Thus, EGFR inhibition induced PI3K/AKT suppression and AMPK activation, both of which can suppress mTORC1 activity (supplementary material, Figure S5). This finding validates the idea that the EGFR signal upregulated by *Elf3* deletion activates mTORC1 activity through PI3K/AKT and AMPK.

Elf3 deletion induces the dedifferentiation and mesenchymal phenotype with EREG/EGFR/mTORC1 upregulation in allograft tumour models

Since KPC and KPCE mice died from pancreatic cancers before gallbladder tumours progressed to invasive

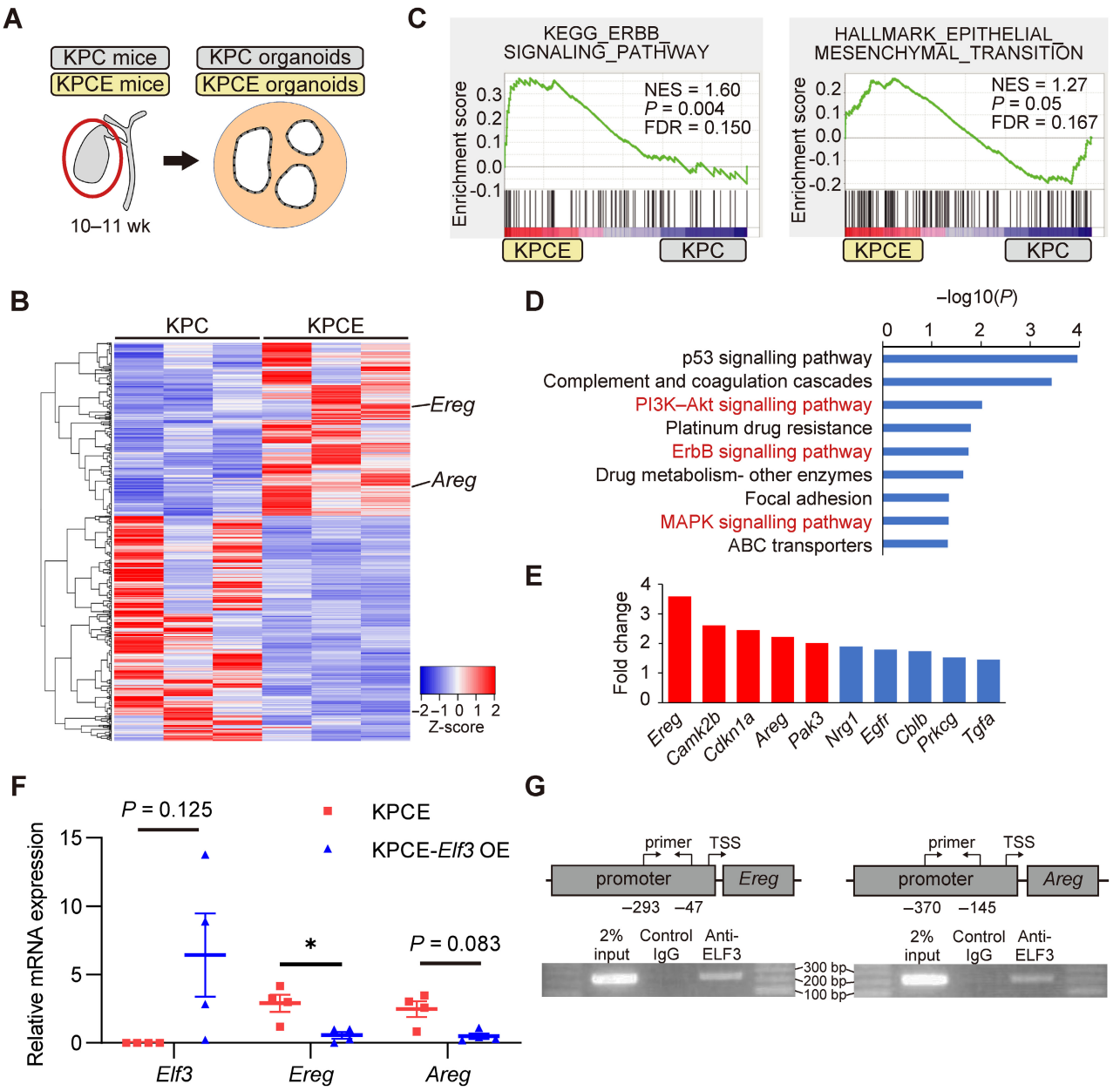

Figure 3. The ERBB signalling pathway is upregulated in KPCE organoids, and ELF3 directly downregulates *Ereg* and *Areg* expression. (A) Organoids were generated from gallbladder of KPC (*Pdx1-Cre*; *Kras*$^{G12D/wt}$; *Trp53*$^{R172H/wt}$; *Elf3*$^{wt/wt}$) and KPCE (*Pdx1-Cre*; *Kras*$^{G12D/wt}$; *Trp53*$^{R172H/wt}$; *Elf3*$^{f/f}$) mice at 10–11 weeks of age. (B) Heat map showing DEGs calculated from RNA-seq data. (C) Enrichment plots from gene set enrichment analysis showing that ERBB and EMT signalling pathways were upregulated in KPCE organoids. The normalised enrichment score (NES), nominal *p* value, and false discovery rate (FDR) are shown in each plot. (D) Upregulated signalling pathways in KPCE organoids analysed through Kyoto Encyclopaedia of Genes and Genomes pathway analysis using DEGs calculated from RNA-seq data. (E) Upregulated genes related to ERBB signalling pathway in KPCE organoids. Red and blue bars show the genes satisfied fold change ≥ 2 and < 2, respectively. (F) RT-qPCR analysis of *Elf3*, *Ereg*, and *Areg* in KPCE and KPCE-*Elf3* OE organoids ($n = 4$ in each group). The expression level of each gene in KPCE and KPCE-*Elf3* OE organoids is shown as a relative ratio to that of KPC organoids ($n = 4$). Means ± SEM. *$P < 0.05$, paired *t*-test. (G) Schematic illustrations showing promoter regions of *Ereg* and *Areg* and PCR primer sets used in ChIP assay, demonstrating that DNA fragments co-precipitated with anti-ELF3 antibody were amplified using PCR using primer sets specific for respective promotor region. TSS, transcription start site.

cancers, we could not evaluate the GBC phenotype under the *Elf3* deletion condition. To overcome this, we generated a subcutaneous allograft mouse model with KPC and KPCE organoids at 16–18 weeks of age (Figure 5A). Although no significant difference in volume was observed between the allograft tumours derived from KPC and KPCE organoids (Figure 5B), histological analysis revealed that allograft KPC-derived tumours had more cystic areas than those in KPCE-derived tumours and the ratio of non-cystic to whole sectional area tended to be greater in KPC than in KPCE allograft tumours, suggesting that the accurate volume of KPCE allograft tumours was larger than that of KPC allograft tumours (Figure 5C). Furthermore, allograft tumours of KPCE organoids showed poorly differentiated structures, whereas allograft tumours of

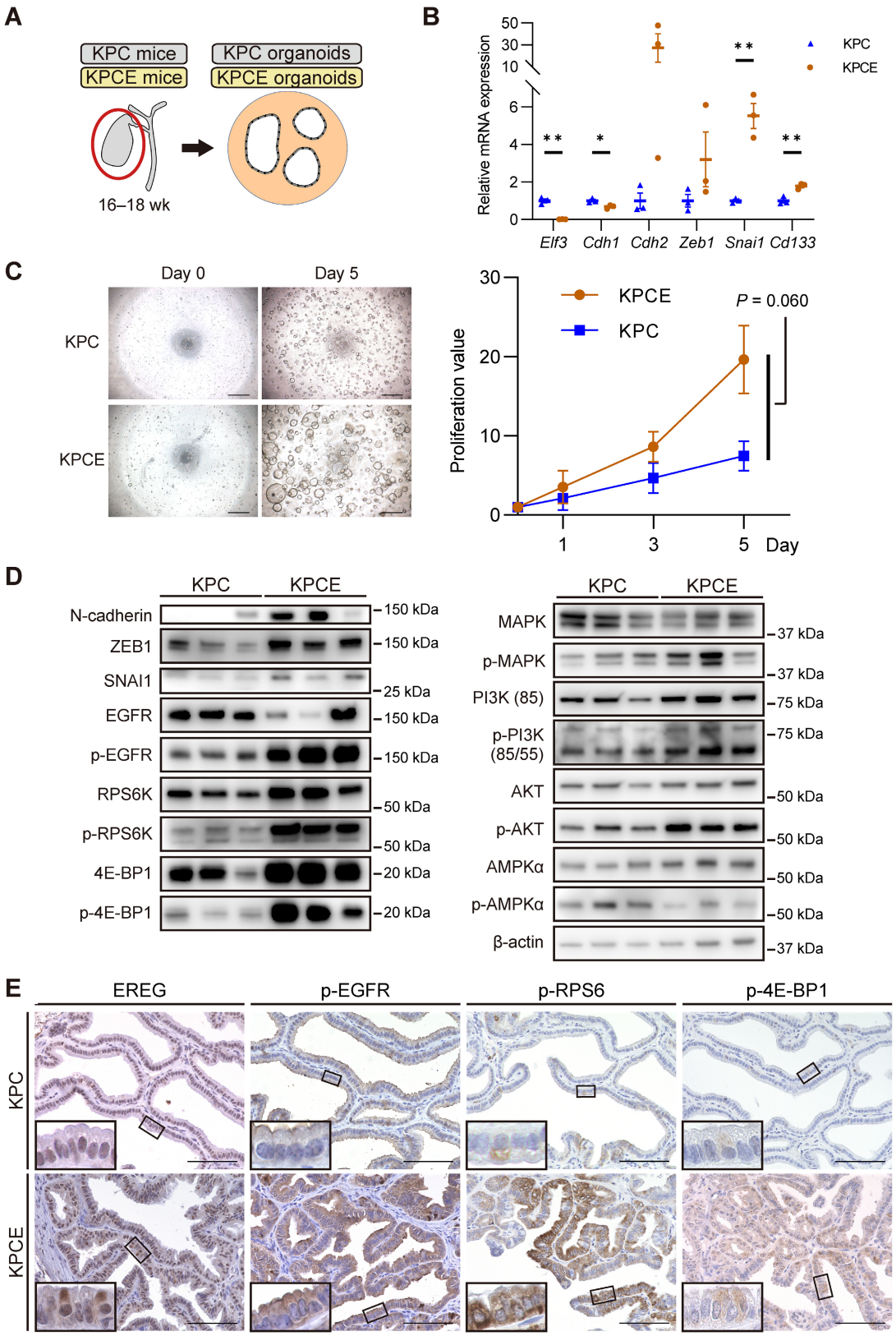

Figure 4. EGFR/mTORC1 signal and EMT are upregulated in KPCE gallbladder tumours. (A) Organoids were generated from gallbladder tissues in KPC (*Pdx1-Cre*; *Kras*$^{G12D/wt}$; *Trp53*$^{R172H/wt}$; *Elf3*$^{wt/wt}$) and KPCE (*Pdx1-Cre*; *Kras*$^{G12D/wt}$; *Trp53*$^{R172H/wt}$; *Elf3*$^{f/f}$) mice at 16–18 weeks of age. (B) RT-qPCR analysis on *Elf3*, an epithelial cell marker gene *Cdh1*, mesenchymal cell marker genes (*Cdh2*, *Zeb1*, and *Snai1*), and a cancer stem cell marker gene *Cd133* in KPC and KPCE organoids ($n = 3$ in each group). Means ± SEM. *$P < 0.05$, **$P < 0.01$, Student's *t*-test. (C) Cell proliferation assay of KPC and KPCE organoids ($n = 3$ in each group). Means ± SEM. Student's *t*-test. (D) Western blot analysis using proteins extracted from KPC and KPCE organoids. (E) Representative immunostaining for EREG, p-EGFR, p-RPS6, and p-4E-BP1 in gallbladder tissues of KPC and KPCE mice. Insets show higher-magnification images. Scale bars, 100 μm.

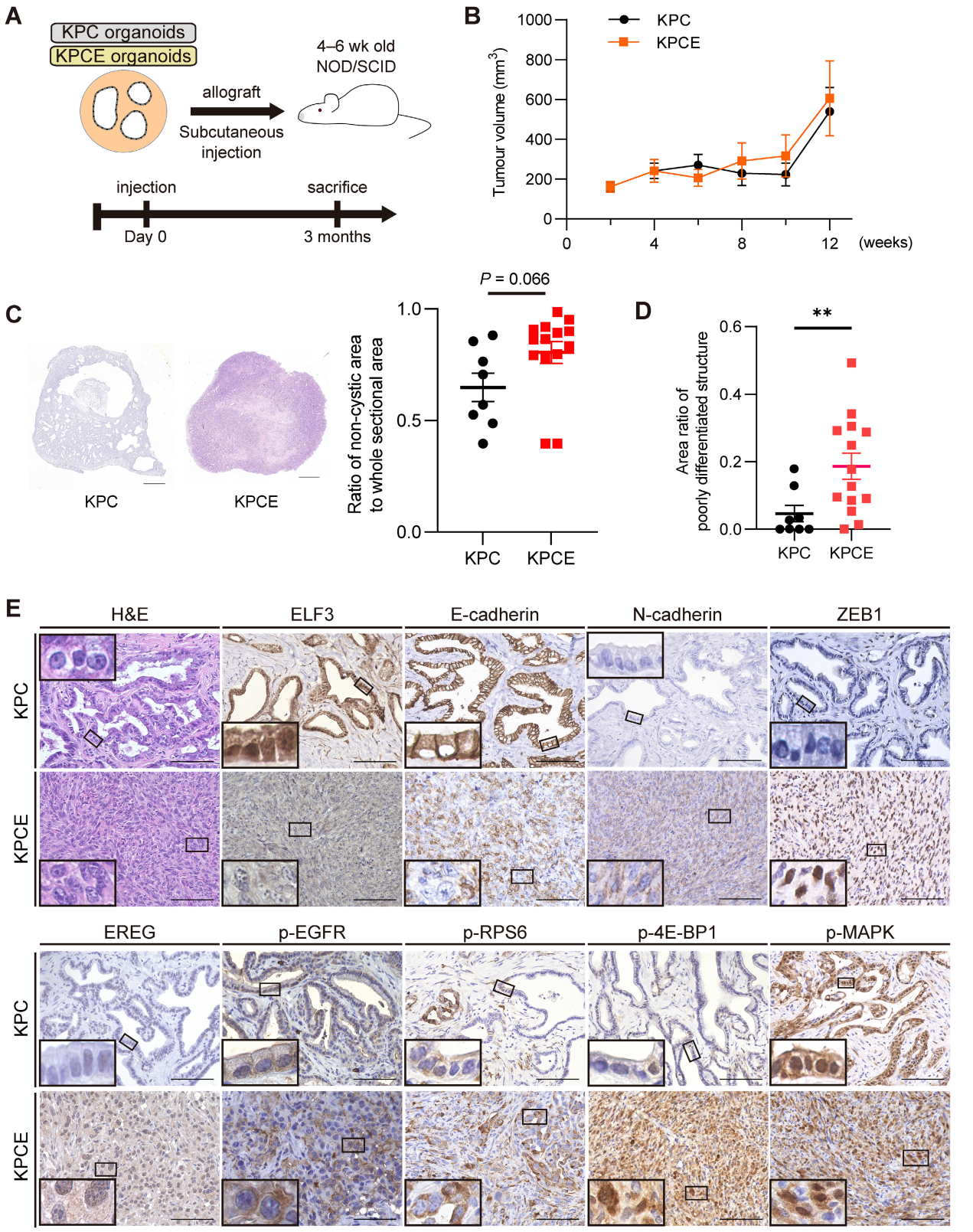

Figure 5. *Elf3* deletion induces dedifferentiation and mesenchymal phenotype with EREG/EGFR/mTORC1 upregulation in allograft tumour models. (A) Schematic illustration of generation method and analysis schedule of allograft mouse model using KPC and KPCE organoids. (B) Graph showing allograft tumour volumes of KPC and KPCE organoids ($n = 6$ and 9 in the KPC and KPCE group, respectively). Means ± SEM are shown. (C) Representative H&E staining of allograft tumour cross sections for KPC and KPCE organoids and quantification of non-cystic to sectional area ratio ($n = 8$ and 14 in KPC and KPCE groups, respectively). Scale bars, 1 mm. Means ± SEM. Student's *t*-test. (D) Representative H&E staining and immunostaining for ELF3, E-cadherin, N-cadherin, ZEB1, EREG, p-EGFR, p-RPS6, p-4E-BP1, and p-MAPK in allograft tumour tissues of KPC and KPCE organoids. Insets show higher-magnification images. Scale bars, 100 μm. (E) Quantification of poorly differentiated structure to sectional area ratio ($n = 8$ and 14 in KPC and KPCE group, respectively). Means ± SEM. $^{**}P < 0.01$, Student's *t*-test.

KPC organoids mainly exhibited tubular structures (Figure 5D,E). IHC on KPCE allograft tumours revealed decreased expression of epithelial cell markers such as E-cadherin and increased expression of mesenchymal cell markers such as N-cadherin and ZEB1 (Figure 5D). IHC also confirmed that EREG, p-EGFR, p-RPS6, and p-4E-BP1 were highly expressed in KPCE allograft tissues compared with those in KPC tissues (Figure 5D). Meanwhile, IHC for phosphorylated MAPK (p-MAPK) expression showed no difference between KPCE and KPC allograft tumours (Figure 5D), although the MAPK signalling pathway was significantly upregulated in KPCE organoids in the pathway analysis, and p-MAPK expression by western blotting tended to be higher in KPCE organoids than in KPC organoids (Figures 3D and 4D).

Additionally, we generated tumour cell lines from both KPC and KPCE allograft tumours and evaluated their cellular properties *in vitro*. KPCE cells showed remarkably higher migration and invasion rates than KPC cells (supplementary material, Figure S6A,B). Furthermore, KPCE cells resulted in more extensive metastases in the livers of allograft mice than KPC cells (supplementary material, Figure S6C). These results indicate that KPCE cells have greater migration, invasion, and metastatic ability than KPC cells. Taken together, these findings suggest that *Elf3* deletion induces dedifferentiation and mesenchymal phenotype in gallbladder tumours in mice.

EREG upregulates the EGFR/mTORC1, and the EREG/EGFR/mTORC1 axis is an important factor in the formation of the mesenchymal structure of KPCE allograft tumours

A previous report revealed that, compared with other EGFR ligands such as EGF and AREG, EREG induces sustained EGFR signalling upregulation [34]. In addition, EREG showed more notable change in its mRNA expression than AREG in our analysis (Figure 3E,F); therefore, we focused on EREG. To elucidate the functional role of EREG in KPCE organoids, we established *Ereg*-knockout KPCE organoids (KPCE-*Ereg* KO) and non-targeting KPCE organoids (KPCE-NT) as controls (Figure 6A). RT-qPCR confirmed that *Ereg* mRNA expression was significantly decreased in KPCE-*Ereg* KO organoids (Figure 6B). Western blotting showed that p-EGFR level was decreased in KPCE-*Ereg* KO organoids, indicating that the ERBB downstream signal was attenuated (Figure 6C). Consistent with this finding, p-4E-BP1 level was decreased in KPCE-*Ereg* KO organoids (Figure 6C). On the other hand, the p-MAPK level was rather increased in KPCE-*Ereg* KO organoids (Figure 6C). In addition, the expression of mesenchymal markers (N-cadherin and SNAI1) decreased in KPCE-*Ereg* KO organoids (Figure 6C). These findings suggest that EREG upregulates the EGFR/mTORC1 pathway, not MAPK, and participates in the induction of EMT in murine gallbladder tumour organoids.

To evaluate the impact of EREG/EGFR/mTORC1 activity on the histological phenotype, we generated subcutaneous allograft mouse models with KPCE-*Ereg* KO and KPCE-NT organoids (Figure 6A). Interestingly, KPCE-*Ereg* KO tumours were significantly smaller than KPCE-NT tumours (Figure 6D). Histological analysis revealed that KPCE-*Ereg* KO tumours mainly showed tubular structures, whereas KPCE-NT tumours showed poorly differentiated structures (Figure 6E). IHC revealed that p-EGFR, p-4E-BP1, and p-RPS6 expression were lower in KPCE-*Ereg* KO tumour tissues than in KPCE-NT tumour tissues (Figure 6E). In addition, IHC showed decreased expression of N-cadherin and ZEB1 in KPCE-*Ereg* KO tumour tissues, indicating that EMT was suppressed in KPCE-*Ereg* KO tumours (Figure 6E). On the other hand, p-MAPK expression in KPCE-*Ereg* KO tumours did not clearly differ from that in KPCE-NT tumours (Figure 6E). These results indicate that the EREG/EGFR/mTORC1 pathway is an important factor in the formation of papillary lesions in the KPCE gallbladder and the mesenchymal structure of KPCE allograft tumours and that the mesenchymal phenotype of KPCE allograft tumours can be at least partially suppressed by *Ereg* deletion.

EGFR/mTORC1 inhibition suppresses cell proliferation and EMT in KPCE organoids

To investigate the pathophysiological role of EGFR/mTORC1 on *Elf3*-deleted organoids, we administered afatinib (an EGFR inhibitor) or rapamycin (mTORC1 inhibitor) to KPCE organoids. Western blotting confirmed suppression of p-EGFR in KPCE organoids treated with afatinib and suppression of phosphorylated RPS6K (p-RPS6K) and p-4E-BP1 in KPCE organoids treated with either drug (supplementary material, Figure S7A). Moreover, western blotting revealed the increased expression of E-cadherin in KPCE organoids treated with afatinib and decreased expression of N-cadherin, ZEB1, and SNAI1 in KPCE organoids treated with either drug, suggesting that EGFR/mTORC1 inhibition suppressed EMT (supplementary material, Figure S7A). In cell proliferation assay, KPCE organoids treated with either drug showed significantly lower proliferation activity than those treated with DMSO (supplementary material, Figure S7B). These results suggest that EGFR/mTORC1 signalling plays an important role in tumour progression and EMT induction in the gallbladder of KPCE mice, suggesting that EGFR/mTORC1 inhibition could be a therapeutic option for GBC with an *Elf3* mutation.

ELF3 regulates *EREG* expression and EGFR/mTOR signalling in human GBC tissues

To determine whether *ELF3* expression affected mTORC1 activity in human GBC tissue, we analysed the RNA-seq data of human GBC published by Pandey *et al* [6]. Most *ELF3* mutations were loss-of-function type; therefore, we divided the samples into wild-type

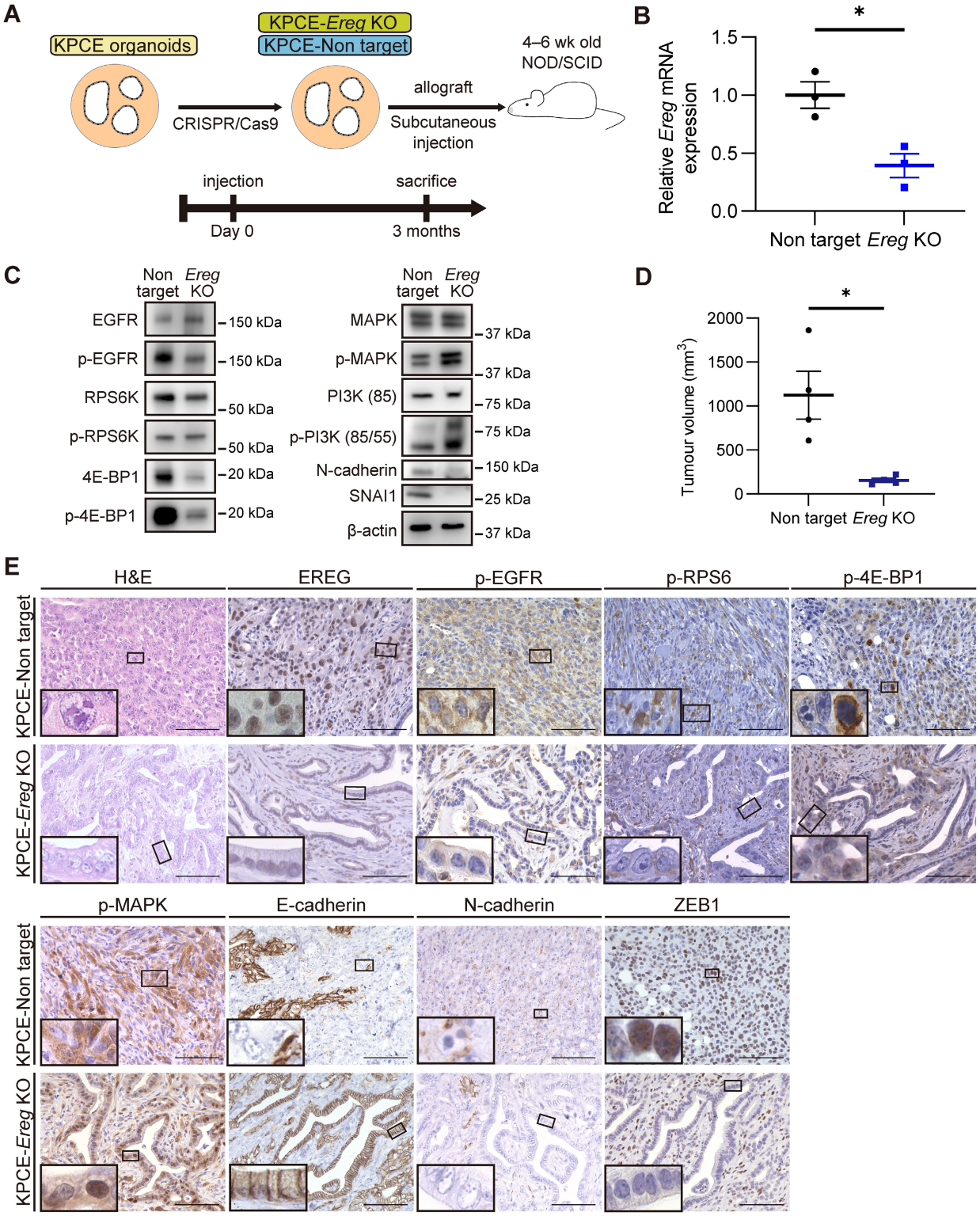

Figure 6. EREG/EGFR/mTORC1 axis is an important factor in the formation of the mesenchymal structure of KPCE allograft tumours. (A) *Ereg*-knockout organoids (KPCE-*Ereg* KO) and negative control organoids (KPCE-NT) were generated from KPCE (*Pdx1-Cre*; *Kras*$^{G12D/wt}$; *Trp53*$^{R172H/wt}$; *Elf3*$^{f/f}$) organoids using CRISPR/Cas9 lentivirus system. An allograft mouse model was generated using the organoids. (B) RT-qPCR analysis of *Ereg* expression in KPCE-*Ereg* KO and KPCE-NT organoids ($n = 3$ each). The expression level of KPCE-*Ereg* KO organoids is shown as a ratio relative to that of KPCE-NT organoids. Means ± SEM. *$P < 0.05$, Student's *t*-test. (C) Western blot analysis of KPCE-*Ereg* KO and KPCE-NT organoids. (D) Volumes of allograft tumours using KPCE-*Ereg* KO and KPCE-NT organoids ($n = 4$ in each group). Means ± SEM. *$P < 0.05$, Student's *t*-test. (E) Representative H&E staining and immunostaining for EREG, p-EGFR, p-RPS6, p-4E-BP1, p-MAPK, E-cadherin, N-cadherin, and ZEB1 in allograft tumour tissues of KPCE-*Ereg* KO and KPCE-NT organoids. Insets show higher-magnification images. Scale bars, 100 μm.

ELF3 (*ELF3*-WT) and mutated *ELF3* (*ELF3*-MT) groups ($n = 92$ and 23, respectively) and analysed the transcript differences between the two groups using GSEA. Consistent with our mouse model data, gene sets related to the EGFR, mTOR, and EMT signalling pathway were significantly enriched in the *ELF3*-MT group

(supplementary material, Figure S8A). Furthermore, there was a mild negative correlation between *ELF3* and *EREG* mRNA expression in the *ELF3*-WT group (supplementary material, Figure S8B). In addition, high *EREG* expression also significantly upregulated the gene sets related to EGFR, mTORC1, and EMT (supplementary material, Figure S8C). These findings suggest that ELF3 regulates *EREG* expression and the EGFR/mTOR signalling pathway in human GBC.

Lastly, we evaluated ELF3/EREG/EGFR/mTORC1 activity in human GBC tissues using IHC. Out of 85 GBC cases, we selected the 47 cases with a T stage of T2 or greater, for which the tissues included both intraepithelial/submucosal portions and invasive portions. We semi-quantitatively evaluated the staining intensities of ELF3, EREG, p-EGFR, and p-4E-BP1 by IHC (supplementary material, Figure S8D) and found that ELF3 expression was significantly reduced in invasive portions compared with that in intraepithelial portions of the tumour. Furthermore, p-4E-BP1 expression was significantly increased, and p-EGFR expression tended to be higher in invasive portions than in intraepithelial/submucosal portions, consistent with our observations with the mouse models. Meanwhile, EREG staining intensity did not differ between intraepithelial/submucosal and invasive portions. Collectively, these results also support the idea that ELF3 regulates EGFR/mTORC1 activity.

Discussion

In this study, we demonstrated that *Elf3* deletion promoted tumour progression and EMT in mice via direct *Ereg* upregulation and subsequent EGFR/mTORC1 signalling pathway activation. Although previous reports showed that ELF3 acted as a tumour suppressor in GBC [6], the underlying molecular mechanism has not been fully elucidated. With the use of an *in vivo* mouse model, this study provides insights into the functional roles of ELF3 in GBC.

We investigated the clinical significance of ELF3 expression in GBC using human samples and showed that low ELF3 expression in GBC was associated with advanced clinical stage and deep tumour invasion. Additionally, the OS of the low ELF3 expression group tended to be shorter than that of the high-ELF3-expression group in human GBC. Consistent with previous reports, these results suggest that ELF3 functions as a tumour suppressor in human GBC development [6,21].

We further analysed the role of ELF3 in GBC using mouse models. *Elf3* deletion resulted in tumour progression in the gallbladder under the condition of *Kras* oncogenic activation and *Trp53* inactivation. Specifically, organoids derived from *Elf3*-deleted gallbladder tumours demonstrated dedifferentiation and EMT. Moreover, transcriptome analysis showed upregulation of the ERBB signalling pathway. In general, alterations in the ERBB family have been identified in various cancers and are involved in cancer progression [9]. Regarding GBC, somatic ERBB family mutations occurred at a rate of 36.8%, and GBC patients with ERBB pathway mutations had a worse outcome [4]. In a mouse model, constitutive ERBB2 expression in gallbladder epithelium led to gallbladder adenocarcinoma development [35]. Considering these reports, ERBB is one of the most important signalling pathways in GBC.

Among the ERBB signalling pathway-related genes, we focused on *Ereg* and found that ELF3 negatively regulated *Ereg* expression via direct interaction with its promoter region. Moreover, *Ereg* deletion suppressed tumour growth and EMT through EGFR/mTORC1 downregulation. EREG is upregulated in various cancers, and its expression correlates with tumour cell growth, invasiveness, and metastasis [36–39]. By contrast, the role of EREG in GBC has not yet been elucidated. Our results suggest that EREG is a key factor for GBC development through EGFR/mTORC1 upregulation, and ELF3 plays an important role by regulating its expression.

To verify the significance of EGFR/mTORC1 in *Elf3*-deleted gallbladder tumours, we administered an inhibitor of EGFR or mTORC1 to KPCE organoids *in vitro*, which suppressed proliferation and EMT in KPCE organoids, suggesting that EGFR/mTORC1 assume a crucial role in development and EMT induction in *Elf3*-deleted gallbladder tumours. Although the therapeutic effect of EGFR or mTORC1 inhibition on human GBC samples was not evaluated in this study, we found that gene sets related to EGFR, mTOR, and EMT were significantly enriched in human GBC with *ELF3* mutations. Moreover, IHC analyses showed that ELF3 deletion was correlated with EGFR/mTORC1 activity and tumour invasion in human GBC tissues. Considering that *Elf3* deletion leads to EGFR/mTORC1 upregulation, EGFR/mTORC1 inhibition can be an effective therapeutic option for human GBC with *ELF3* alterations. However, further investigation is essential to verify the therapeutic effects in human GBC.

Concerning the EREG/EGFR/mTORC1 axis, some issues remain unelucidated in this study. First, the mTOR signal is frequently activated in human GBC, and high mTOR activation is correlated with the invasive and migratory capacity of GBC cell lines and poor prognosis of human GBC patients [40,41]; however, the molecular mechanism by which mTORC1 induces EMT has not been fully clarified. A previous report revealed that loss of 4E-BP1 function induced EMT via translational activation of SNAI1, which repressed E-cadherin expression and was, thus, considered a key regulator of EMT [42]. In our study, *Snai1* mRNA and SNAI1 expression was higher in KPCE than in KPC organoids. In addition, *Ereg* deletion or EGFR/mTORC1 inhibition in KPCE organoids decreased SNAI1 expression. These results suggest that SNAI1 might play an important role in inducing EMT as the downstream molecule of the EREG/EGFR/mTORC1 axis in KPCE organoids.

Further studies on the relationship between mTORC1 and EMT are needed. Second, AMPK activity was downregulated in KPCE organoids; however, the molecular interaction between AMPK and the ELF3/EREG/EGFR axis has not yet been elucidated. In lung cancer, inhibition of the EGFR tyrosine kinase inhibits glucose uptake and reduces intracellular ATP levels through liver kinase B1 (LKB1), which induces AMPK activation [43], consistent with our results. Therefore, EGFR signalling might suppress AMPK activation through LKB1 downregulation. Because EGFR activity was upregulated in the KPCE organoids in our study, EGFR activation might also induce AMPK suppression in gallbladder tumours. However, the role of AMPK and its association with the ELF3/EREG/EGFR axis in GBC requires further investigation. Third, EREG is a ligand of EGFR, and EREG loss can induce downregulation of MAPK and mTORC1 signalling. Upon comparing KPC and KPCE organoids, we found that both MAPK and mTORC1 were upregulated in KPCE organoids; however, MAPK was upregulated in KPCE-*Ereg* KO organoids, in contrast to mTORC1. This contradiction could be explained by the MAPK-mTORC1 feedback loop. A previous report revealed that mTORC1 inhibition led to MAPK activation through a PI3K-dependent feedback loop [44]. In our study, phosphorylated PI3K was upregulated in KPCE-*Ereg* KO organoids (Figure 6C), indicating that MAPK was activated through the negative feedback loop. Furthermore, in the allograft mouse models using KPCE-*Ereg* KO and KPCE-NT organoids, mTORC1 rather than MAPK was suggested to play an important role in inducing EMT. On the other hand, EGFR inhibition, which led to the inhibition of both MAPK and mTORC1, induced E-cadherin upregulation and N-cadherin downregulation compared with mTORC1 inhibition alone in the *in vitro* inhibitor experiment of KPCE organoids, suggesting that EMT was suppressed more through dual inhibition of MAPK and mTORC1 than through mTORC1 inhibition alone. This indicates that MAPK may also play an important role in EMT. It is clear from our and previous findings that the MAPK and mTORC1 signalling pathways have an intimate and complicated relationship and are important factors in GBC, which warrants a more detailed investigation of these pathways. Fourth, unlike p-EGFR and p-4E-BP1, EREG staining intensity did not differ in comparison between intraepithelial/submucosal and invasive portions in human GBC tissues. While this result is contradictory to the result of human GBC RNA-seq data, it suggests that molecules other than EREG, such as AREG or EGF, might also play important roles between ELF3 and EGFR/mTORC1 in human GBC, and further study on human GBC is essential.

To develop tumours in the murine gallbladder, we induced oncogenic *Kras*^{G12D} and *Trp53*^{R172H} mutation. *TP53* is the most frequently mutated gene in GBC, and *KRAS* mutation is observed in 4–8% of cases, and several altered genes have been identified in the ERBB/RAS/PI3K pathway [4,6]. Therefore, we believe that this combination of gene mutations satisfyingly imitates the mutation profile of human GBC. Whereas these mutations could lead to the development of precancerous lesions in gallbladder, the mice harbouring these mutations died from pancreatic cancers before gallbladder lesions progressed into advanced cancers. As an alternative method, we used a subcutaneously implanted allograft mouse model. This model could generate invasive cancers derived from KPC and KPCE organoids. However, this approach has the demerit of changes in the tumour growth environment, which is also a limitation of our study. Therefore, establishment of a well-refined GBC mouse model is needed.

In conclusion, we have demonstrated that ELF3 functions as a tumour suppressor in a gallbladder tumour mouse model by directly downregulating *Ereg* expression and consequently downregulating the EGFR/mTORC1 signalling pathway. Further studies are warranted to elucidate the functional role of ELF3 in human GBC.

Acknowledgements

We thank Yuta Kawamata and Taichi Ito for their technical support. We also thank Editage (www.editage.com) for the English language editing. Cell lysate sonication using a Covaris S220 Focused Ultrasonicator was performed at the Medical Research Support Center, Graduate School of Medicine, Kyoto University. This work was supported by JSPS and MEXT KAKENHI (Grants 19K16711, 20H03659, 21J15798, 21K19480, and 22K15528); A-MED P-CREATE (Grant 21cm0106375h); A-MED P-PROMOTE (Grant 22ama221515h); JST Moonshot Research and Development Program (Grant JPMJMS2022); and JST COI-NEXT Grant JPMJPF2018.

Author contributions statement

TN, YN and MS conceived and designed the study. TN performed all the experiments and analysed the data with the assistance of YN, MS, MY, S Mat, YM, SO, HY, HO, TK, S Mar, T Mat and T Mar. TN analysed the clinical data with the assistance of YN. TN and HT performed the sequence analysis and interpreted the data. TN wrote the manuscript, and YN and MS revised it. NU, EH, YK and HS supervised the study. All authors had final approval of the submitted manuscript.

Data availability statement

The data of RNA-seq performed in this study are publicly available in DNA Data Bank of Japan Sequence Read Archive (https://ddbj.nig.ac.jp/resource/sra-submission/DRA014895). The other data generated in this study are available from the corresponding author upon reasonable request.

References

1. Wistuba I, Gazdar AF. Gallbladder cancer: lessons from a rare tumour. *Nat Rev Cancer* 2004; **4:** 695–706.
2. Hundal R, Shaffer EA. Gallbladder cancer: epidemiology and outcome. *Clin Epidemiol* 2014; **6:** 99–109.
3. Zhu X, Zhang X, Hu X, *et al*. Survival analysis of patients with primary gallbladder cancer from 2010 to 2015: a retrospective study based on SEER data. *Medicine (Baltimore)* 2020; **99:** e22292.
4. Li M, Zhang Z, Li X, *et al*. Whole-exome and targeted gene sequencing of gallbladder carcinoma identifies recurrent mutations in the ErbB pathway. *Nat Genet* 2014; **46:** 872–876.
5. Nakamura H, Arai Y, Totoki Y, *et al*. Genomic spectra of biliary tract cancer. *Nat Genet* 2015; **47:** 1003–1010.
6. Pandey A, Stawiski EW, Durinck S, *et al*. Integrated genomic analysis reveals mutated ELF3 as a potential gallbladder cancer vaccine candidate. *Nat Commun* 2020; **11:** 4225.
7. Zhang H, Berezov A, Wang Q, *et al*. ErbB receptors: from oncogenes to targeted cancer therapies. *J Clin Invest* 2007; **117:** 2051–2058.
8. Wang Z. ErbB receptors and cancer. *Methods Mol Biol* 2017; **1652:** 3–35.
9. Yarden Y, Pines G. The ERBB network: at last, cancer therapy meets systems biology. *Nat Rev Cancer* 2012; **12:** 553–563.
10. Arteaga CL, Engelman JA. ERBB receptors: from oncogene discovery to basic science to mechanism-based cancer therapeutics. *Cancer Cell* 2014; **25:** 282–303.
11. Yachida S, Wood LD, Suzuki M, *et al*. Genomic sequencing identifies ELF3 as a driver of ampullary carcinoma. *Cancer Cell* 2016; **29:** 229–240.
12. Sizemore GM, Pitarresi JR, Balakrishnan S, *et al*. The ETS family of oncogenic transcription factors in solid tumours. *Nat Rev Cancer* 2017; **17:** 337–351.
13. Luk IY, Reehorst CM, Mariadason JM. ELF3, ELF5, EHF and SPDEF transcription factors in tissue homeostasis and cancer. *Molecules* 2018; **23:** 2191.
14. Wang JL, Chen ZF, Chen HM, *et al*. Elf3 drives β-catenin transactivation and associates with poor prognosis in colorectal cancer. *Cell Death Dis* 2014; **5:** e1263.
15. Ali SA, Justilien V, Jamieson L, *et al*. Protein kinase Cι drives a NOTCH3-dependent stem-like phenotype in mutant *KRAS* lung adenocarcinoma. *Cancer Cell* 2016; **29:** 367–378.
16. Gingras MC, Covington KR, Chang DK, *et al*. Ampullary cancers harbor ELF3 tumor suppressor gene mutations and exhibit frequent WNT dysregulation. *Cell Rep* 2016; **14:** 907–919.
17. Yeung TL, Leung CS, Wong KK, *et al*. ELF3 is a negative regulator of epithelial-mesenchymal transition in ovarian cancer cells. *Oncotarget* 2017; **8:** 16951–16963.
18. Wang H, Yu Z, Huo S, *et al*. Overexpression of ELF3 facilitates cell growth and metastasis through PI3K/Akt and ERK signaling pathways in non-small cell lung cancer. *Int J Biochem Cell Biol* 2018; **94:** 98–106.
19. Zheng L, Xu M, Xu J, *et al*. ELF3 promotes epithelial-mesenchymal transition by protecting ZEB1 from miR-141-3p-mediated silencing in hepatocellular carcinoma. *Cell Death Dis* 2018; **9:** 387.
20. Enfield KSS, Marshall EA, Anderson C, *et al*. Epithelial tumor suppressor ELF3 is a lineage-specific amplified oncogene in lung adenocarcinoma. *Nat Commun* 2019; **10:** 5438.
21. Suzuki M, Saito-Adachi M, Arai Y, *et al*. E74-like factor 3 is a key regulator of epithelial integrity and immune response genes in biliary tract cancer. *Cancer Res* 2021; **81:** 489–500.
22. Gu G, Dubauskaite J, Melton DA. Direct evidence for the pancreatic lineage: NGN3+ cells are islet progenitors and are distinct from duct progenitors. *Development* 2002; **129:** 2447–2457.
23. Jackson EL, Willis N, Mercer K, *et al*. Analysis of lung tumor initiation and progression using conditional expression of oncogenic K-ras. *Genes Dev* 2001; **15:** 3243–3248.
24. Olive KP, Tuveson DA, Ruhe ZC, *et al*. Mutant p53 gain of function in two mouse models of Li-Fraumeni syndrome. *Cell* 2004; **119:** 847–860.
25. Fukuda A, Kawaguchi Y, Furuyama K, *et al*. Loss of the major duodenal papilla results in brown pigment biliary stone formation in pdx1 null mice. *Gastroenterology* 2006; **130:** 855–867.
26. Chung WC, Wang J, Zhou Y, *et al*. $Kras^{G12D}$ upregulates notch signaling to induce gallbladder tumorigenesis in mice. *Onco Targets Ther* 2017; **4:** 131–138.
27. Hingorani SR, Wang L, Multani AS, *et al*. $Trp53^{R172H}$ and $Kras^{G12D}$ cooperate to promote chromosomal instability and widely metastatic pancreatic ductal adenocarcinoma in mice. *Cancer Cell* 2005; **7:** 469–483.
28. Seino T, Kawasaki S, Shimokawa M, *et al*. Human pancreatic tumor organoids reveal loss of stem cell niche factor dependence during disease progression. *Cell Stem Cell* 2018; **22:** 454–467.e6.
29. Sampaziotis F, Muraro D, Tysoe OC, *et al*. Cholangiocyte organoids can repair bile ducts after transplantation in the human liver. *Science* 2021; **371:** 839–846.
30. Berasain C, Avila MA. Amphiregulin. *Semin Cell Dev Biol* 2014; **28:** 31–41.
31. Riese DJ 2nd, Cullum RL. Epiregulin: roles in normal physiology and cancer. *Semin Cell Dev Biol* 2014; **28:** 49–56.
32. Kim LC, Cook RS, Chen J. mTORC1 and mTORC2 in cancer and the tumor microenvironment. *Oncogene* 2017; **36:** 2191–2201.
33. Mungai PT, Waypa GB, Jairaman A, *et al*. Hypoxia triggers AMPK activation through reactive oxygen species-mediated activation of calcium release-activated calcium channels. *Mol Cell Biol* 2011; **31:** 3531–3545.
34. Freed DM, Bessman NJ, Kiyatkin A, *et al*. EGFR ligands differentially stabilize receptor dimers to specify signaling kinetics. *Cell* 2017; **171:** 683–695.e18.
35. Kiguchi K, Carbajal S, Chan K, *et al*. Constitutive expression of ErbB-2 in gallbladder epithelium results in development of adenocarcinoma. *Cancer Res* 2001; **61:** 6971–6976.
36. Zhu Z, Kleeff J, Friess H, *et al*. Epiregulin is up-regulated in pancreatic cancer and stimulates pancreatic cancer cell growth. *Biochem Biophys Res Commun* 2000; **273:** 1019–1024.
37. Gupta GP, Nguyen DX, Chiang AC, *et al*. Mediators of vascular remodelling co-opted for sequential steps in lung metastasis. *Nature* 2007; **446:** 765–770.
38. Shigeishi H, Higashikawa K, Hiraoka M, *et al*. Expression of epiregulin, a novel epidermal growth factor ligand associated with prognosis in human oral squamous cell carcinomas. *Oncol Rep* 2008; **19:** 1557–1564.
39. Zhang J, Iwanaga K, Choi KC, *et al*. Intratumoral epiregulin is a marker of advanced disease in non-small cell lung cancer patients and confers invasive properties on EGFR-mutant cells. *Cancer Prev Res (Phila)* 2008; **1:** 201–207.
40. Zong H, Yin B, Zhou H, *et al*. Inhibition of mTOR pathway attenuates migration and invasion of gallbladder cancer via EMT inhibition. *Mol Biol Rep* 2014; **41:** 4507–4512.
41. Yang D, Chen T, Zhan M, *et al*. Modulation of mTOR and epigenetic pathways as therapeutics in gallbladder cancer. *Mol Ther Oncolytics* 2021; **20:** 59–70.
42. Cai W, Ye Q, She QB. Loss of 4E-BP1 function induces EMT and promotes cancer cell migration and invasion via cap-dependent translational activation of snail. *Oncotarget* 2014; **5:** 6015–6027.
43. Cheng FJ, Chen CH, Tsai WC, *et al*. Cigarette smoke-induced LKB1/AMPK pathway deficiency reduces EGFR TKI sensitivity in NSCLC. *Oncogene* 2021; **40:** 1162–1175.

44. Carracedo A, Ma L, Teruya-Feldstein J, *et al*. Inhibition of mTORC1 leads to MAPK pathway activation through a PI3K-dependent feedback loop in human cancer. *J Clin Invest* 2008; **118:** 3065–3074.
45. Kim D, Langmead B, Salzberg SL. HISAT: a fast spliced aligner with low memory requirements. *Nat Methods* 2015; **12:** 357–360.
46. Pertea M, Pertea GM, Antonescu CM, *et al*. StringTie enables improved reconstruction of a transcriptome from RNA-seq reads. *Nat Biotechnol* 2015; **33:** 290–295.
47. Robinson MD, McCarthy DJ, Smyth GK. edgeR: a Bioconductor package for differential expression analysis of digital gene expression data. *Bioinformatics* 2010; **26:** 139–140.
48. Mootha VK, Lindgren CM, Eriksson KF, *et al*. PGC-1alpha-responsive genes involved in oxidative phosphorylation are coordinately downregulated in human diabetes. *Nat Genet* 2003; **34:** 267–273.
49. Subramanian A, Tamayo P, Mootha VK, *et al*. Gene set enrichment analysis: a knowledge-based approach for interpreting genome-wide expression profiles. *Proc Natl Acad Sci U S A* 2005; **102:** 15545–15550.
50. Huang DW, Sherman BT, Lempicki RA. Systematic and integrative analysis of large gene lists using DAVID bioinformatics resources. *Nat Protoc* 2009; **4:** 44–57.
51. Sherman BT, Hao M, Qiu J, *et al*. DAVID: a web server for functional enrichment analysis and functional annotation of gene lists (2021 update). *Nucleic Acids Res* 2022; **50:** W216–W221.
52. Yoshida K, Sanada M, Shiraishi Y, *et al*. Frequent pathway mutations of splicing machinery in myelodysplasia. *Nature* 2011; **478:** 64–69.
53. Yoshizato T, Dumitriu B, Hosokawa K, *et al*. Somatic mutations and clonal hematopoiesis in aplastic anemia. *N Engl J Med* 2015; **373:** 35–47.
54. Sun J, Nishiyama T, Shimizu K, *et al*. TCC: an R package for comparing tag count data with robust normalization strategies. *BMC Bioinformatics* 2013; **14:** 219.

References 45–54 are cited only in the supplementary material.

SUPPLEMENTARY MATERIAL ONLINE

Supplementary materials and methods

Figure S1. Gene recombination in extrahepatic biliary epithelial cells confirmed using X-gal staining in biliary tract of *Pdx1-Cre*; *Rosa26*$^{LSL\text{-}LacZ}$ mice

Figure S2. ELF3 is not essential for development and maintenance of extrahepatic biliary tract in mice

Figure S3. *Elf3* deletion does not cause tumour formation in gallbladder in context of *Trp53* mutation in mice

Figure S4. Genotyping and RT-qPCR analysis for verification of origin of organoids

Figure S5. EGFR signalling regulates mTORC1 activity through PI3K/AKT and AMPK

Figure S6. Dedifferentiation and epithelial–mesenchymal transition (EMT) are induced in KPCE allograft tumour cells *in vitro*

Figure S7. EGFR/mTORC1 inhibition suppresses cell proliferation and EMT in KPCE organoids

Figure S8. Gene sets related to EGFR, mTOR, and EMT are significantly enriched in human GBC tissues with ELF3 mutations

Table S1. Clinical information of 85 patients with GBC

Table S2. Antibodies for IHC, western blotting, and ChIP assay used in this study

Table S3. Primer sets for RT-qPCR, ChIP, and genotyping analyses used in this study

ELF3 suppresses gallbladder cancer development through downregulation of the EREG/EGFR/mTOR complex 1 signalling pathway

T Nakamura *et al. J Pathol* https://doi.org/10.1002/path.6144

Supplementary material online

Supplementary Figures S1–S8

Supplementary Tables S1 provided as a separate Excel file

Supplementary Tables S2, S3

Supplementary materials and methods

Reference numbers refer to the main text list.

Allograft mouse models

For the subcutaneous tumour model, 10 and 15 NOD.CB17-*Prkdc*^{scid}/Jcl mice at 4–6 weeks of age were used in the *Pdx1-Cre*; *Kras*^{G12D}; *Trp53*^{R172H}; *Elf3*$^{wt/wt}$ (KPC) and *Pdx1-Cre*; *Kras*^{G12D}; *Trp53*^{R172H}; *Elf3*$^{f/f}$ (KPCE) group, respectively. Organoid cells (1×10^6) were suspended in 100 µl medium and growth factor-reduced Matrigel (BD Biosciences, San Jose, CA, USA, #356230) (1:1 mixture) and subcutaneously injected into a flank.

For the liver metastasis model, three NOD.CB17-*Prkdc*^{scid}/Jcl mice at 4–6 weeks of age were used

in each group. Allograft tumour cells (5×10^5) were suspended in 50 µl of medium and injected into the spleen. After 4 weeks, the mice were sacrificed using CO_2. Liver metastases and whole liver areas were manually measured using ImageJ software (version 1.53f, National Institutes of Health, Bethesda, MD, USA, RRID: SCR_003070) from the maximum sectioned surface of each lobe, and the ratio of each total was calculated. All cell injection procedures were performed under anaesthesia and analgesia with isoflurane (Wako, Osaka, Japan, #099-06571) and buprenorphine (Sigma-Aldrich, St. Louis, MO, USA, #BP1062), respectively.

Histology

Mouse tissues were fixed in 10% neutral phosphate-buffered formalin, embedded in paraffin wax, and cut into 5-µm-thick sections. The sections were stained with haematoxylin (Sigma-Aldrich) and eosin (Wako) for histological analysis. For immunohistochemistry (IHC), antigen retrieval was performed by boiling the sections in either 10 mM citric acid buffer (pH 6.0) or EDTA buffer (pH 8.0). After blocking in blocking solution (Dako, Santa Clara, CA, USA, #X0909), the sections were incubated with primary antibodies overnight at 4 °C. Immunoperoxidase labelling was performed using the EnVision+ kit (Dako, #K4001 and #K4003) or the VECTASTAIN Elite ABC kit (Vector Laboratories, Burlingame, CA, USA, #PK-6105). The sections were stained with Liquid DAB+ Substrate Chromogen System (Dako, #K3468), followed by counterstaining with haematoxylin. For 5-bromo-4-chloro-3-indolyl-β-D-galactoside (X-gal) staining, fresh tissues

were fixed for 1 h at 4 °C in PBS containing 4% paraformaldehyde, 5 mM EGTA, 2 mM $MgCl_2$, 0.2% glutaraldehyde, and 0.02% NP-40. The tissues were then incubated with the staining substrate [PBS containing 5 mM $K_3Fe(CN)_6$, 5 mM $K_4Fe(CN)_6$, 2 mM $MgCl_2$, 0.02% NP-40, 0.1% sodium deoxycholate, and 1 mg/ml X-gal] overnight at 20–26 °C. After fixation and paraffin embedding, the sections were counterstained using Nuclear Fast Red (ScyTek Laboratories, Logan, UT, USA, #NFS500). Detailed information for the antibodies used is provided in supplementary material, Table S2.

In the histological analysis of the gallbladder, we calculated the occupancy rate of papillary lesions in the gallbladder lumen using ImageJ as follows: 1 –inner-gallbladder cavity area/area enclosed by outermost layer of gallbladder wall.

Organoids and cell lines

Organoids were established from murine tissues as follows. The murine gallbladder was detached carefully from the gallbladder bed of the liver and then resected by cutting the cystic duct. The common bile duct between the junction of the cystic and common hepatic duct and the upper edge of the pancreas were resected. Resected tissues were washed in PBS, minced into small pieces, and digested with 1 mg/ml collagenase D (Roche, Basel, Switzerland, #11088866001) suspended in DMEM (Thermo Fisher Scientific, Waltham, MA, USA, #11965092) for 15 min at 37 °C. The tissue suspension was then passed through a 100-μm cell strainer, washed with DMEM

supplemented with 10% FBS (Gibco, Dublin, Ireland), and embedded in Matrigel. For organoid culture, advanced DMEM/F12 (Thermo Fisher Scientific, #12634010) was supplemented with 1% penicillin/streptomycin antibiotic stock solution (Thermo Fisher Scientific, #15140122), 10 mM HEPES (Thermo Fisher Scientific, #15630080), 1% GlutaMAX (Thermo Fisher Scientific, #35050061), 1 mM *N*-acetyl-L-cysteine (Sigma-Aldrich, #PHR1098), B27 (Thermo Fisher Scientific, #17504044), 10 mM nicotinamide (Sigma-Aldrich, #N-3376), and 10 μM Y-27632 (Tocris Bioscience, Bristol, UK, #1254). For the drug administration experiments, afatinib (Tokyo Chemical Industry, Tokyo, Japan, #A2870) and rapamycin (LC laboratories, Woburn, MA, USA, #R-5000) were dissolved in DMSO (Wako, #049-07213) and added to the medium at concentrations of 1 and 10 μM, respectively. The proteins were extracted from the organoids after a 6-h incubation. Organoids were passaged every 5–7 days, depending on their growth, during which the Matrigel was dissolved by incubation in TrypLE (Thermo Fisher Scientific, #12605036) for 10 min at 37 °C. After washing with DMEM, the cells were centrifuged at 300 × *g* for 5 min and resuspended and embedded in Matrigel. Cell lines were cultured in advanced DMEM/F12 supplemented with 1% penicillin/streptomycin stock solution and 1% GlutaMAX. All organoids and cell lines were cultured at 37 °C under 5% CO_2. The primers used for genotyping are listed in supplementary material, Table S3.

Lentivirus transfection

For lentiviral production, 7–8 × 10^6 HEK293T cells were transfected with pCAG-HIVgp and pCMV-VSV-G-RSV-Rev lentiviral packaging plasmids (#RDB04394 and #RDB04393, provided by RIKEN BRC through the National BioResource Project, Japan) and lentiviral transfer plasmids. The lentiviral transfer plasmids were produced using Gateway™ LR clonase™ Enzyme Mix (Thermo Fisher Scientific, #10694223) from CSII-EF-RfA-IRES-Puro (#RDB12869, provided by RIKEN BRC) and pDONR221-Elf3 (for Elf3 overexpression, produced by Thermo Fisher Scientific) plasmids. For *Ereg* deletion, the CRISPR/Cas9 system was used. Vector plasmids for *Ereg* deletion (#GSGM11941-24865803) and non-target deletion (#GSGC11953) were purchased from Horizon Discovery (Cambridge, UK). The transfected HEK293T cells were cultured for 48 h. The culture supernatants were collected, filtered, concentrated using PEG-it Virus Precipitation solution (System Biosciences, Palo Alto, CA, USA, #LV810A-1), and resuspended in PBS. For infection, cell pellets were resuspended in medium containing 5 μg/ml polybrene and viral solution, and the cell suspension was centrifuged at 1000 × *g* for 30 min at 32 °C.

RNA isolation and RNA sequencing (RNA-seq)

RNA was extracted using RNeasy Mini Kit (QIAGEN, Hilden, Germany, #74104). Library construction and sequencing were performed by Macrogen Japan (Tokyo, Japan) using TruSeq Stranded mRNA Library Prep Kit (Illumina, San Diego, CA, USA, #20020594) and NovaSeq 6000 platform (Illumina, RRID: SCR_016387). Raw reads were aligned to the reference genome

sequence (GRCm38/mm10) using HISAT2 (RRID: SCR_015530) [45], and the total mapped raw read numbers were calculated using Stringtie (RRID: SCR_016323) [46]. The normalized mRNA expression level of each gene was calculated using the trimmed mean of the M-values algorithm, and differentially expressed genes (DEGs) were extracted using the edgeR program (RRID: SCR_012802) in the default setting [47]. Gene set enrichment analysis (GSEA) was performed using GSEA software (RRID: SCR_003199) and the Molecular Signature Database (RRID: SCR_016863) provided by the Broad Institute of MIT and Harvard [48,49]. DEGs were defined as genes satisfying expression |fold change| ≥ 2 and exact paired *t*-test raw *P*-value < 0.05. Pathway analysis for the DEGs was performed using DAVID 2021 (RRID: SCR_001881) [50,51]. The RNA-seq data generated in this study are publicly available in the DNA Data Bank of Japan Sequence Read Archive under Accession No. DRA014895.

Western blot analysis

Organoids were homogenized in cell lysis buffer (Cell Signaling Technology, Danvers, MA, USA, #9803) supplemented with protease inhibitor cocktail (Cell Signaling Technology, #5871) and PhosSTOP (Roche, #4906837001). The protein extracts were boiled in Laemmli sample buffer (Bio-Rad, Tokyo, Japan, #1610747) supplemented with 2.5% mercaptoethanol, fractionated on sodium dodecyl sulphate polyacrylamide gel (Bio-Rad, #4561086), and transferred to polyvinylidene difluoride membranes (Bio-Rad, #1620174). After blocking with 10% dry

skimmed milk in PBS, the membranes were incubated with primary antibodies overnight at 4 °C, followed by incubation with secondary antibodies. SuperSignal West Femto Maximum Sensitivity Substrate (Thermo Fisher Scientific, #0034095) was used to visualize the protein bands using a Trans-Blot® Turbo™ system (Bio-Rad, RRID: SCR_019036) following the manufacturer's instructions. Detailed information on the antibodies used is provided in supplementary material, Table S2.

RT-qPCR

Single-strand cDNA was synthesized from the extracted RNA using ReverTra Ace qPCR RT Master Mix (Toyobo, Osaka, Japan, #FSQ-201). RT-qPCR was performed using SYBR Green Master Mix (Roche, #4312704) and a LightCycler 480 platform (Roche, RRID: SCR_012155). The expression level of the indicated genes was standardized according to the expression level of *Gapdh*. The primers used are listed in supplementary material, Table S3.

ChIP

ChIP was performed using a SimpleChIP Plus Enzymatic Chromatin IP Kit (Cell Signaling Technology, #502050909) following the manufacturer's instructions. Input DNA was collected from the sheared chromatin before immunoprecipitation. Immunoprecipitation was performed with normal rabbit IgG (provided in the kit) as a control and anti-ELF3 antibody (Thermo Fisher

Scientific, #PA5-47776, 1:500). The antibodies and primers are listed in Table S2 and S3, respectively. Primer sets were designed such that the amplified sequences included the binding motif of the ETS domain (GGAA/T)—a DNA-binding domain shared by all members of the ETS family, including ELF3.

Cell proliferation assay

Cell proliferation assay was performed using PrestoBlue Cell Viability Reagent (Thermo Fisher Scientific, #A13262) following the manufacturer's instructions. In brief, organoids (5×10^3 cells/well) were seeded in 96-well plates. The absorbance at 570 and 595 nm was measured using a plate reader after 1-h incubation with the medium containing the reagent. The proliferation values were calculated as follows: (absorbance at 570 nm of organoid-containing well – absorbance at 595 nm of organoid-containing well) − (absorbance at 570 nm of empty well − absorbance at 595 nm of empty well)/(absorbance at 570 nm of organoid-containing well on day 0 – absorbance at 595 nm of organoid-containing well on day 0) − (absorbance at 570 nm of empty well on day 0 − absorbance at 595 nm of empty well on day 0).

Scratch assay

The cells were seeded in 6-cm dishes and grown into a confluent monolayer. After washing with PBS, the cells were incubated in DMEM containing 0.5% FBS for 24 h. After scratching with a

200-μl micropipette tip, cells were incubated in DMEM containing 0.5% FBS. Cell migration was measured 24 h after scratching. The wound closure percentage was quantified using ImageJ software. Three replicates were performed for each experiment.

Invasion assay

Invasion assays were performed using a Corning BioCoat Matrigel Invasion Chamber (Corning, Corning, NY, USA) in 24-well plates, according to the manufacturer's instructions. In brief, cells (1.5×10^5 cells/well) were seeded in serum-free DMEM in the upper chambers, and the bottom chambers were filled with DMEM containing 10% FBS. After a 30-h incubation, cells that penetrated the membrane were fixed with methanol and stained with haematoxylin. The number of invading cells was manually counted from middle-power magnification (×200) images. The mean score was calculated from the three images.

Analysis of human GBC RNA-seq data

The RNA-seq data for human GBC were obtained from The European Genome-Phenome Archive (Accession No.: EGAS00001003004) [6]. Each FASTQ file was aligned to the reference genome sequence (GRCh37/hg19), and the total mapped raw read numbers were calculated using the Genomon RNA pipeline [52,53]. The normalized mRNA expression level of each gene was calculated using the trimmed mean of M-values algorithm with the TCC package

(RRID:SCR_001779) [54], and the DEGs were determined using edgeR in the default setting.

Supplementary Figures S1–S8

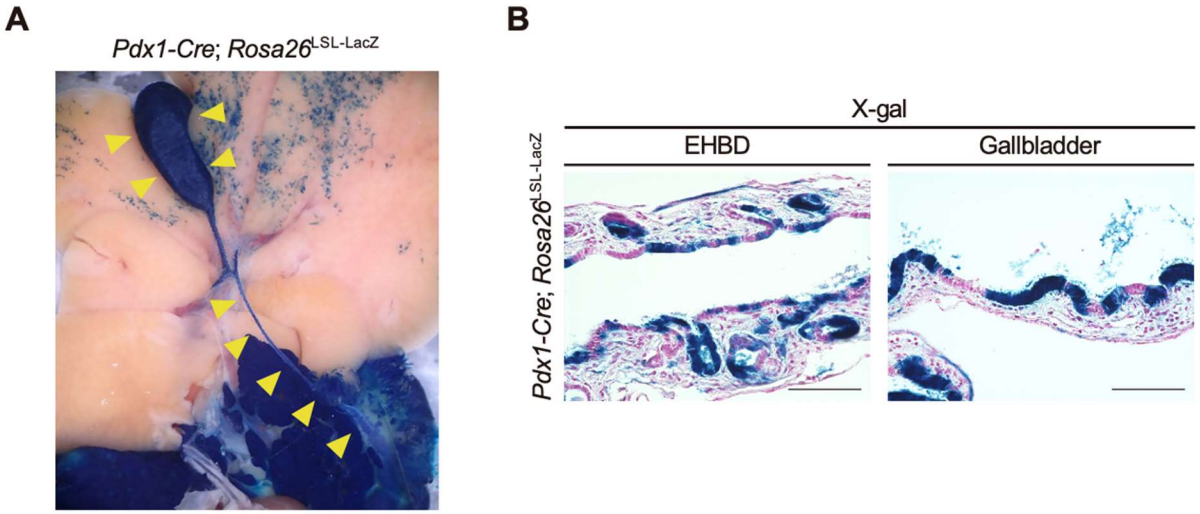

Figure S1. Gene recombination in extrahepatic biliary epithelial cells confirmed using X-gal staining in the biliary tract of *Pdx1-Cre; Rosa26*$^{LSL\text{-}LacZ}$ mice.

(A) Gross appearance of extrahepatic biliary duct (EHBD) and gallbladder of *Pdx1-Cre; Rosa26*$^{LSL\text{-}LacZ}$ mice at 4 weeks of age with X-gal staining. Yellow arrowheads indicate EHBD and gallbladder. (B) X-gal staining in EHBD and gallbladder tissues of *Pdx1-Cre; Rosa26*$^{LSL\text{-}LacZ}$ mice at 4 weeks of age. Scale bars, 100 μm.

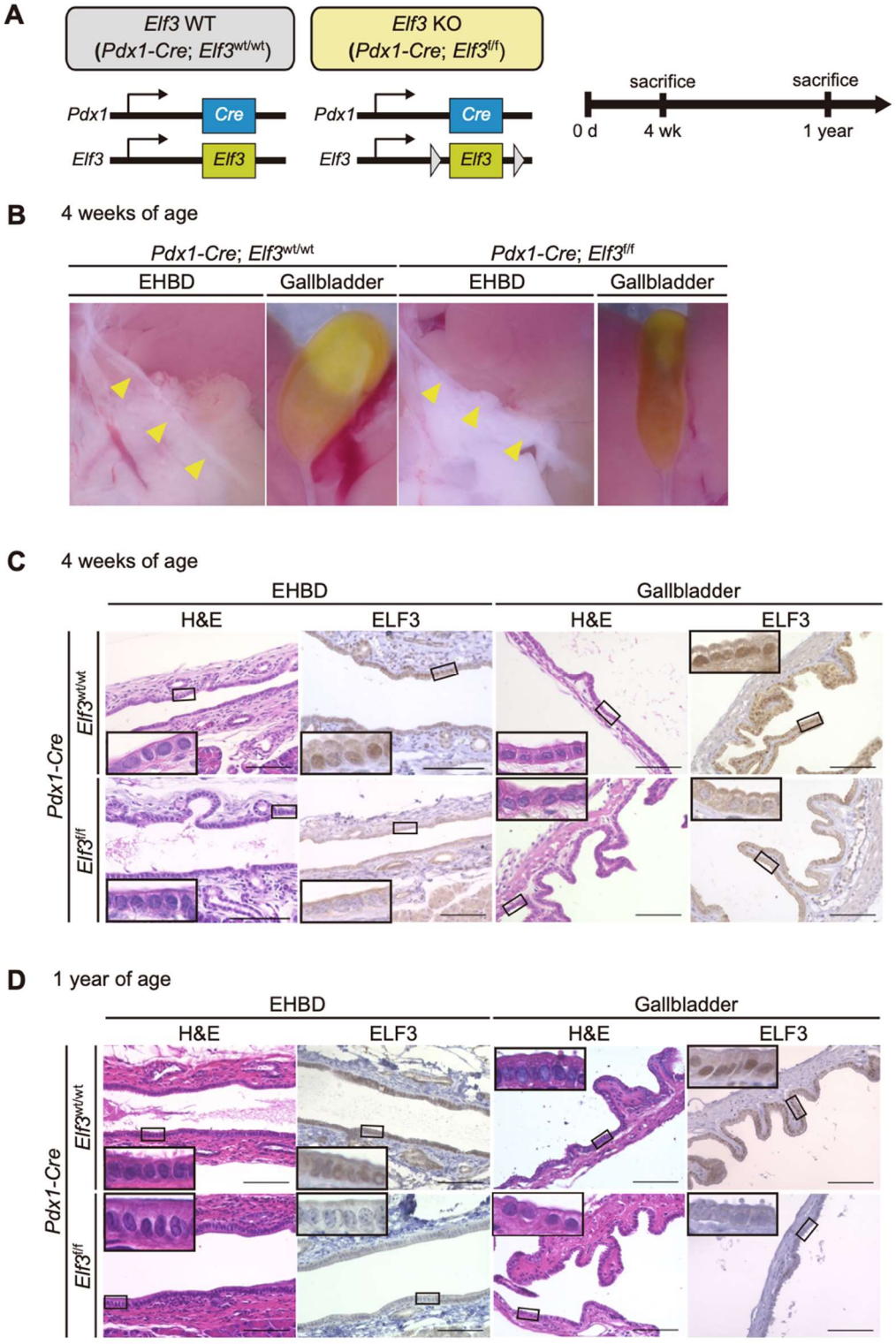

Figure S2. ELF3 is not essential for development and maintenance of extrahepatic biliary tract in mice. (A) Genetic design of *Elf3* WT (*Pdx1-Cre; Elf3*$^{wt/wt}$) and *Elf3* KO (*Pdx1-Cre; Elf3*$^{f/f}$) mice. Arrowheads indicate loxP sites. (B) Gross appearance of EHBD and gallbladder of *Elf3* WT and KO mice at 4 weeks of age. Yellow arrowheads indicate EHBD. (C–D) H&E staining and immunostaining for ELF3 in EHBD and gallbladder tissues of *Elf3* WT and KO mice at 4 weeks (C) and 1 year (D) of age. The insets show high-magnification images. Scale bars, 100 μm.

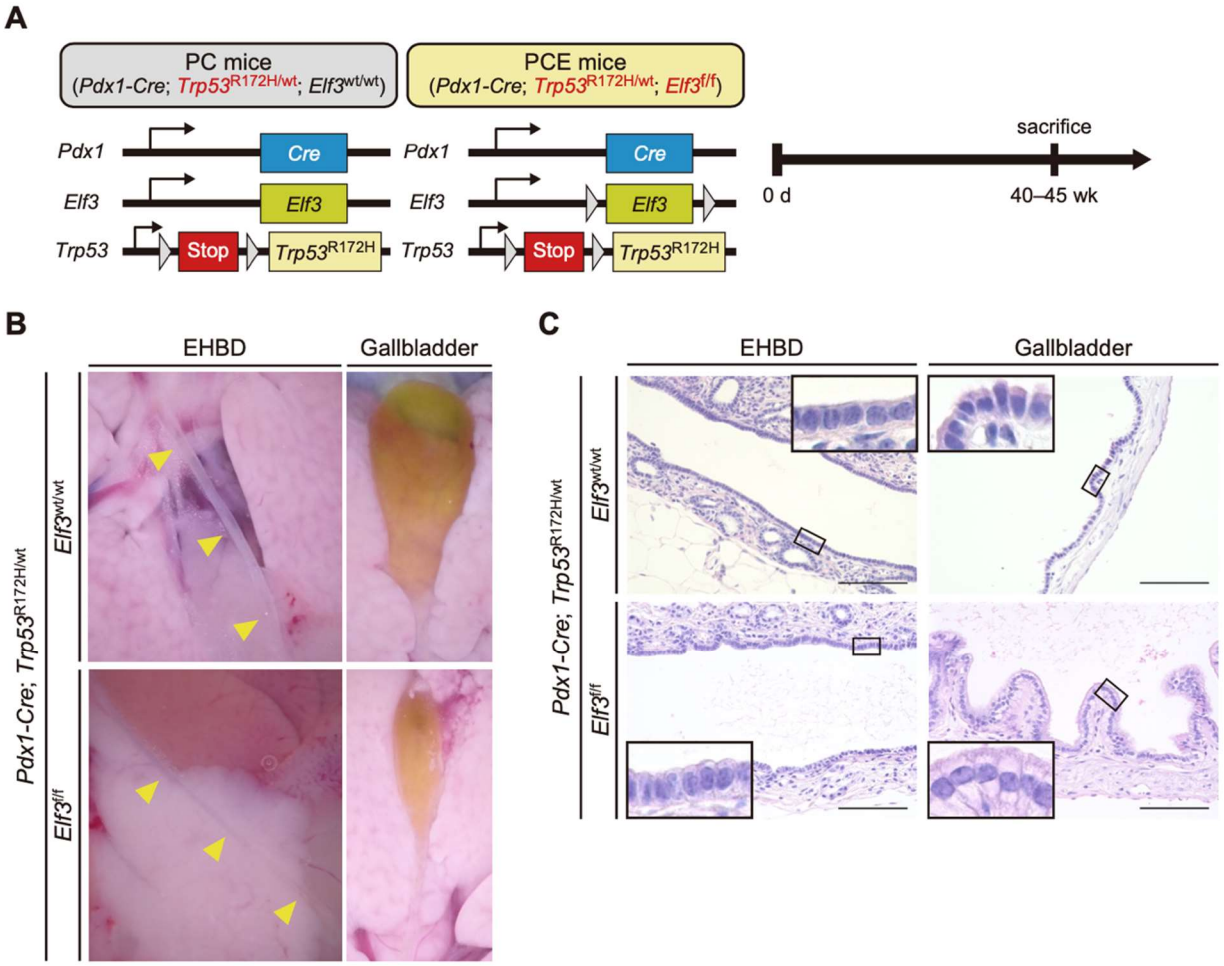

Figure S3. *Elf3* deletion does not cause tumour formation in gallbladder in context of *Trp53* mutation in mice. (A) Genetic design of PC (*Pdx1-Cre; Trp53*$^{R172H/wt}$*; Elf3*$^{wt/wt}$) and PCE mice (*Pdx1-Cre; Trp53*$^{R172H/wt}$*; Elf3*$^{f/f}$). Arrowheads indicate loxP sites. Cre-mediated deletion induces a monoallelic mutation in *Trp53* and biallelic deletion of *Elf3*. (B) Gross appearance of EHBD and gallbladder of PC and PCE mice at 40–45 weeks of age. Yellow arrowheads indicate EHBD. (C) H&E staining in EHBD and gallbladder tissues of PC and PCE mice at 40–45 weeks of age. Insets show higher-magnification images. Scale bars, 100 μm.

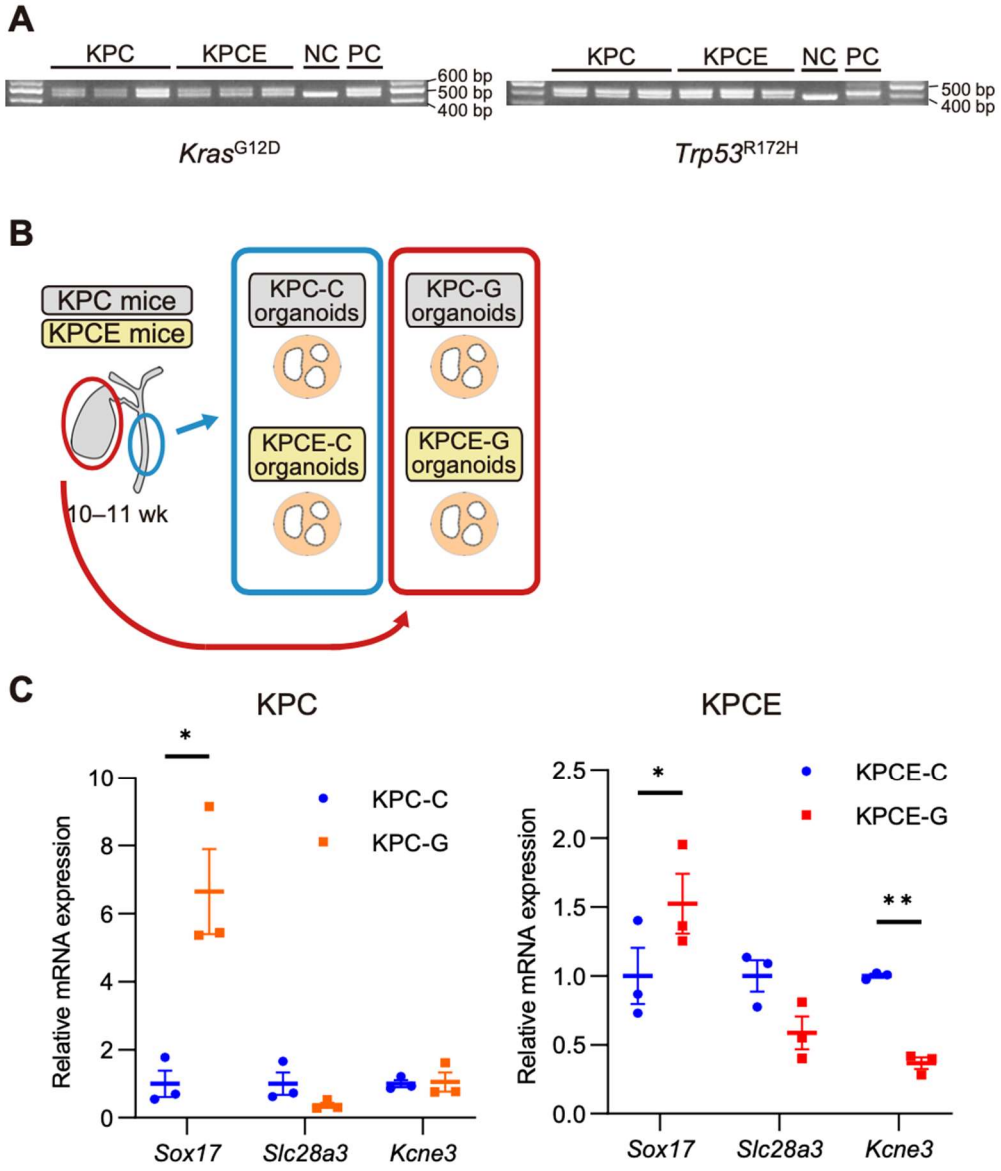

Figure S4. Genotyping and RT-qPCR analysis verifying origins of organoids. (A) Genotyping of recombined *Kras*^{G12D} and *Trp53*^{R172H} alleles in KPC (*Pdx1-Cre; Kras*$^{G12D/wt}$*; Trp53*$^{R172H/wt}$*; Elf3*$^{wt/wt}$) and KPCE (*Pdx1-Cre; Kras*$^{G12D/wt}$*; Trp53*$^{R172H/wt}$*; Elf3*$^{f/f}$) organoids ($n = 3$ in each group). DNA for negative control (NC) and positive control (PC) was extracted from tail of a KPC mouse and pancreatic cancer cell line derived from KPC mouse, respectively. (B) Organoids were generated separately from gallbladder and common bile duct tissues of KPC and KPCE mice at 10–11 weeks of age. KPC-C, organoids derived from common bile duct of KPC mice; KPC-G, organoids derived from gallbladder of KPC mice; KPCE-C, organoids derived from common bile duct of KPCE mice; KPCE-G, organoids derived from gallbladder of KPCE mice. (C) RT-qPCR analysis of *Sox17*, *Slc28a3*, and *Kcne3* expression in KPC-C, KPC-G, KPCE-C, and KPCE-G organoids ($n = 3$ in each group). Means ± SEM. *$p < 0.05$, **$p < 0.01$, Student's t-test.

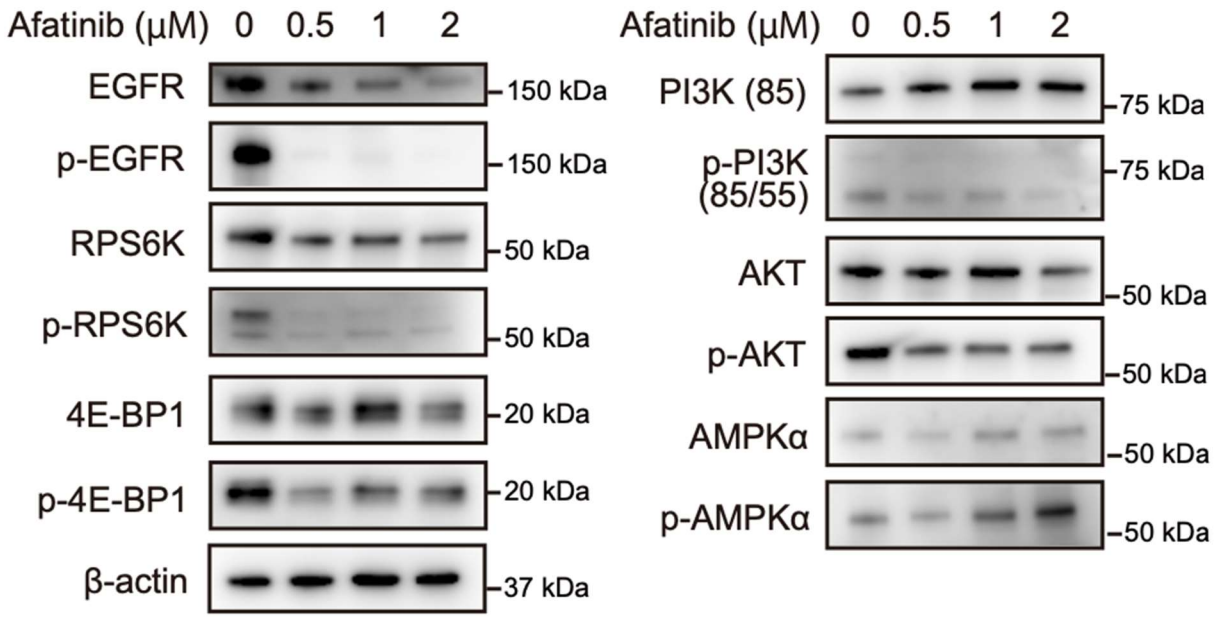

Figure S5. EGFR signalling regulates mTORC1 activity through PI3K/AKT and AMPK. Western blot analysis of KPCE organoids cultured with EGFR inhibitor afatinib.

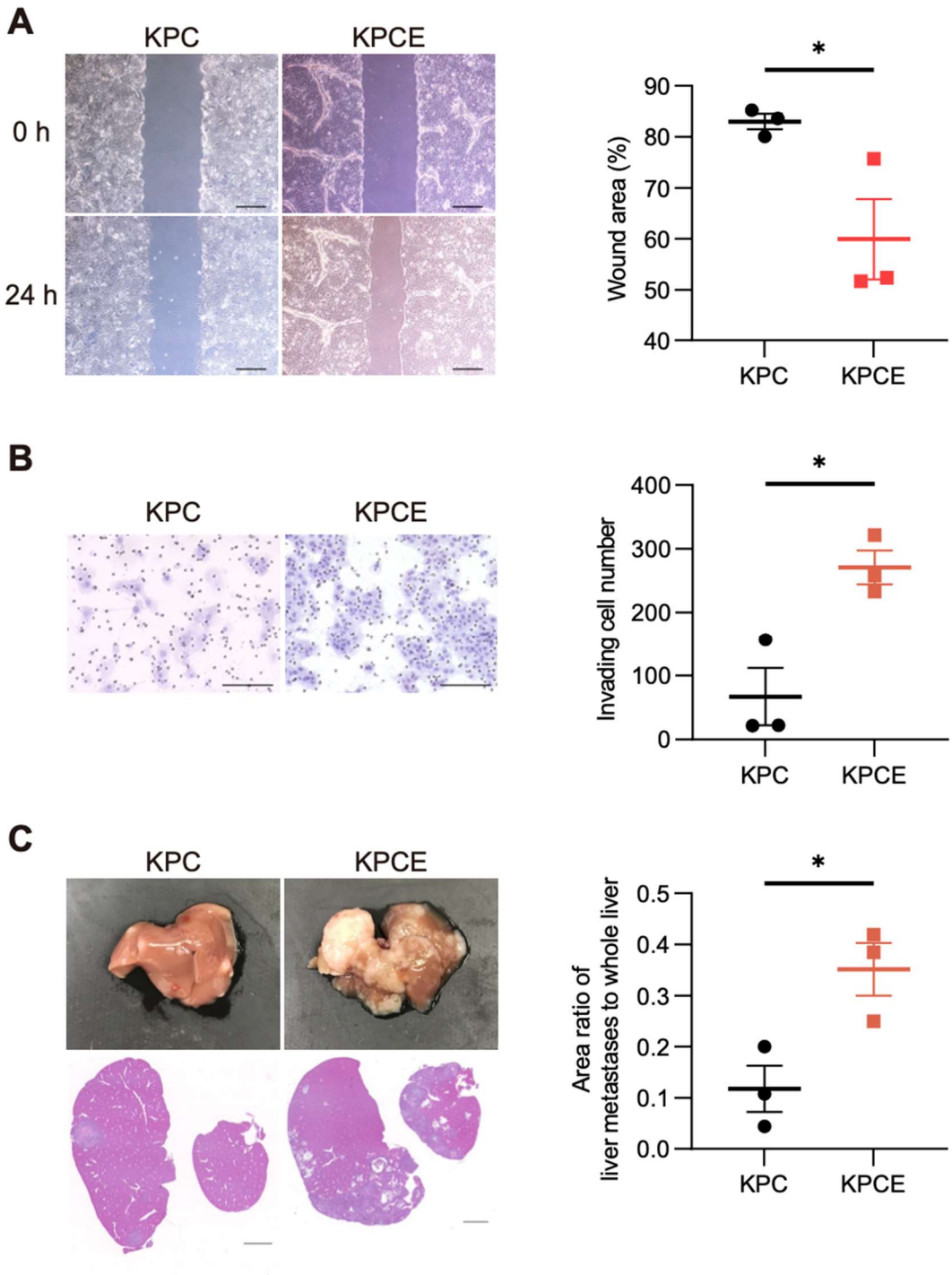

Figure S6. Dedifferentiation and epithelial–mesenchymal transition (EMT) are induced in KPCE allograft tumour cells *in vitro*. (A) Representative images and quantification of wound areas in scratch assay (n = 3 in each group). Means ± SEM. Scale bars, 500 μm. *$p < 0.05$, Student's t-test. (B) Representative images and quantification of invaded cells in invasion assay (n = 3 in each group). Means ± SEM. Scale bars, 200 μm. *$p < 0.05$, Student's t-test. (C) Representative images (macrographs and sectional views at low magnification, scale bars, 1 mm)

and area ratios of liver metastases to whole liver ($n = 3$ in each group). Means ± SEM. *$p < 0.05$, Student's *t*-test.

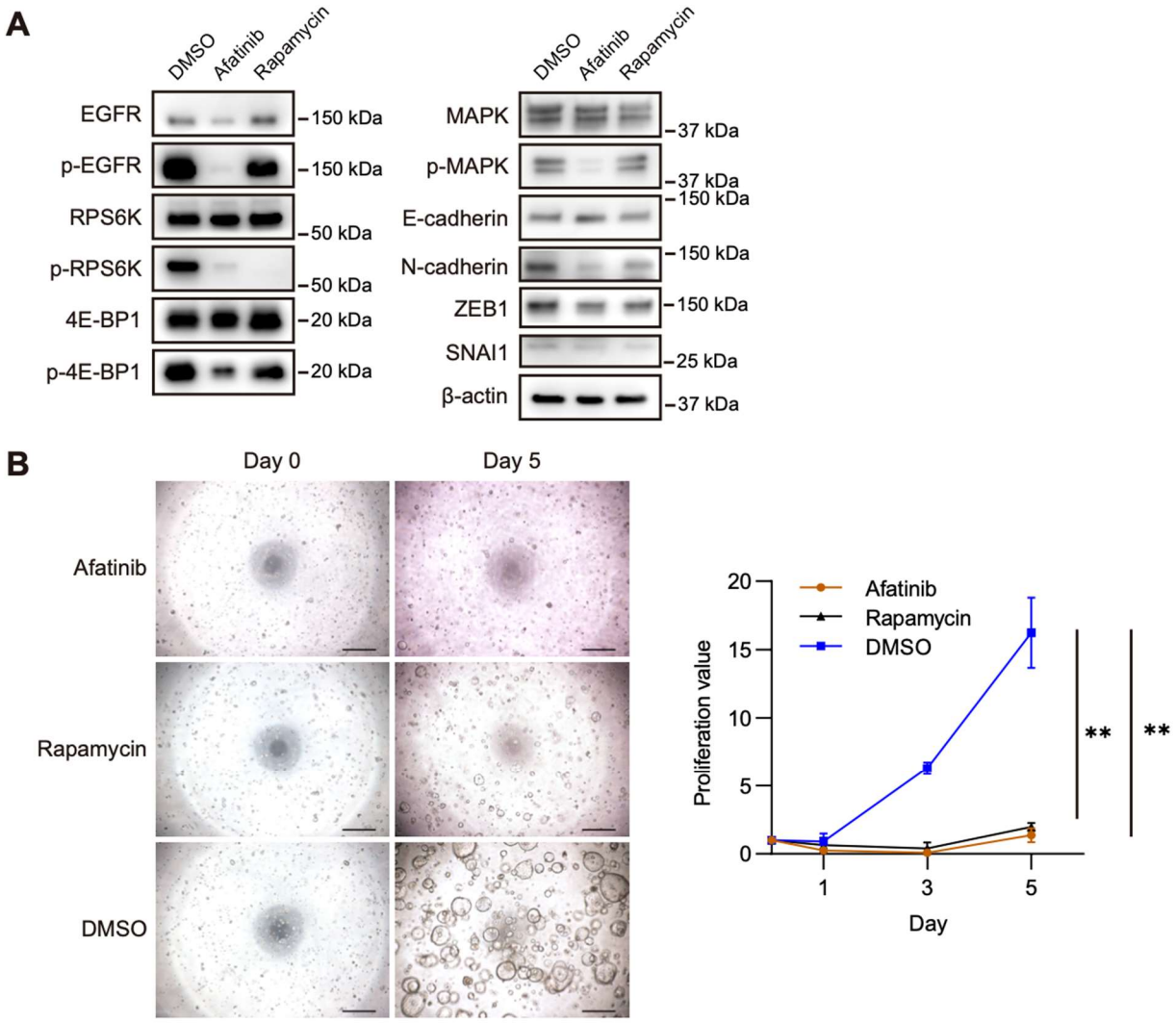

Figure S7. EGFR/mTORC1 inhibition suppresses cell proliferation and EMT in KPCE organoids. (A) Western blot analysis of KPCE (*Pdx1-Cre; Kras*$^{G12D/wt}$*; Trp53*$^{R172H/wt}$*; Elf3*$^{f/f}$) organoids treated with afatinib, rapamycin, or DMSO. (B) Cell proliferation assay of KPCE organoids treated with afatinib, rapamycin, or DMSO ($n = 3$ in each group). Proliferation values were calculated as follows: (absorbance at 570 nm of organoid-containing well − absorbance at 595 nm of organoid-containing well) − (absorbance at 570 nm of empty well – absorbance at 595 nm of empty well)/(absorbance at 570 nm of organoid-containing well on day 0 − absorbance at 595 nm of organoid-containing well on day 0) − (absorbance at 570 nm of empty well on day 0 − absorbance at 595 nm of empty well on day 0). Means ± SEM. $^{**}p < 0.01$, one-way ANOVA test.

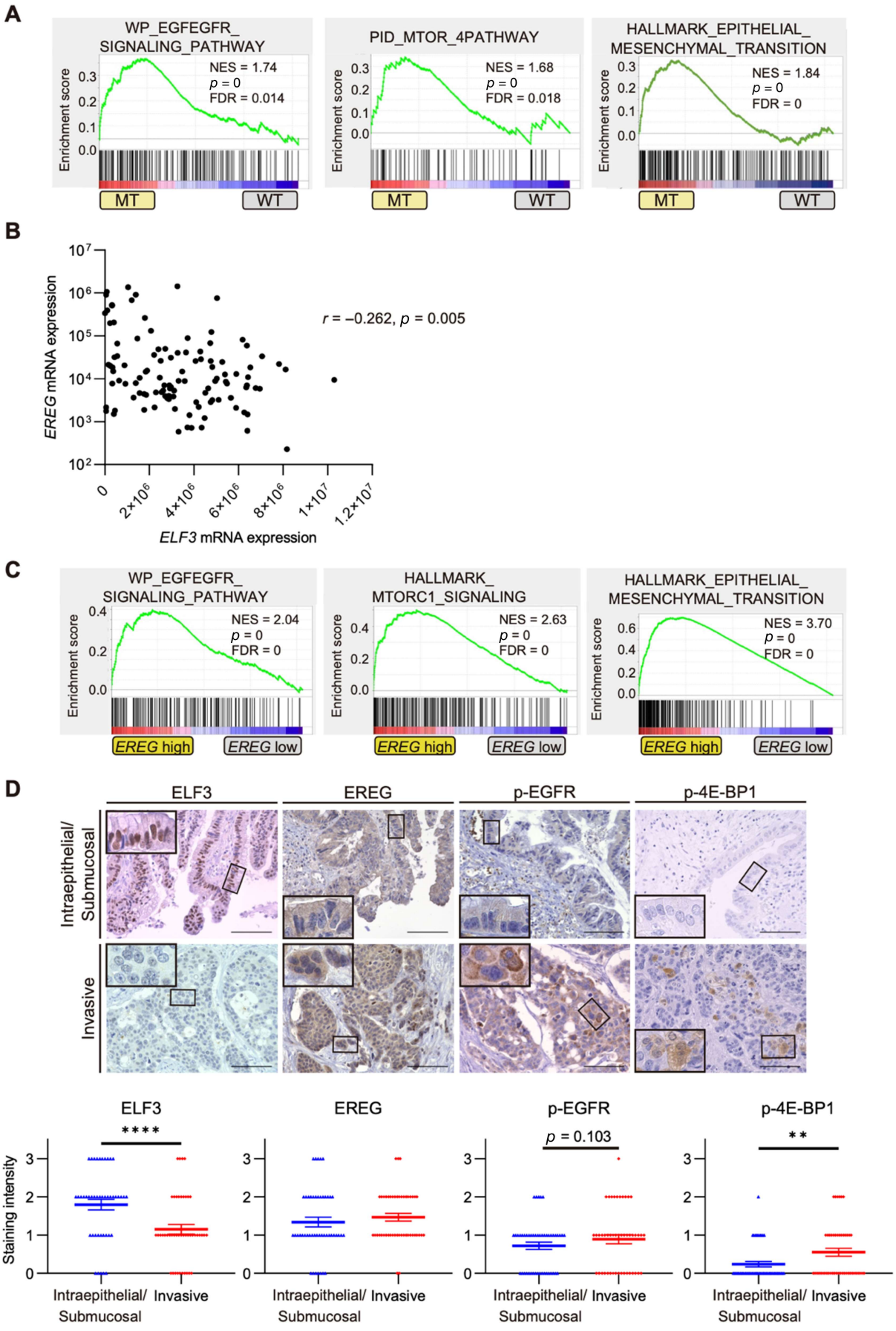
A
WP_EGFEGFR_ SIGNALING_PATHWAY
NES = 1.74
p = 0
FDR = 0.014
PID_MTOR_4PATHWAY
NES = 1.68
p = 0
FDR = 0.018
HALLMARK_EPITHELIAL_ MESENCHYMAL_TRANSITION
NES = 1.84
p = 0
FDR = 0
Enrichment score
MT
WT
B
EREG mRNA expression
ELF3 mRNA expression
r = –0.262, p = 0.005
C
WP_EGFEGFR_ SIGNALING_PATHWAY
NES = 2.04
p = 0
FDR = 0
HALLMARK_ MTORC1_SIGNALING
NES = 2.63
p = 0
FDR = 0
HALLMARK_EPITHELIAL_ MESENCHYMAL_TRANSITION
NES = 3.70
p = 0
FDR = 0
EREG high
EREG low
D
ELF3
EREG
p-EGFR
p-4E-BP1
Intraepithelial/ Submucosal
Invasive
Staining intensity
****
p = 0.103
**
Intraepithelial/ Submucosal
Invasive

Figure S8. Gene sets related to EGFR, mTOR, and EMT are significantly enriched in human GBC tissues with *ELF3* mutations. (A) Enrichment plots from GSEA showing that the signalling pathways related to EGFR, mTOR, and EMT were upregulated in mutated *ELF3* (*ELF3*-MT) group (n = 23) in comparison with those in wild-type ELF3 (*ELF3*-WT) group (n = 93). Normalized enrichment score (NES), nominal p value, and false discovery rate (FDR) are shown in each plot. (B) Dot plot showing correlation between *ELF3* and *EREG* mRNA expression in human GBC tissues (n = 113). Correlation coefficient (r) = –0.262; p = 0.005. (C) Enrichment plots from GSEA showing that the signalling pathways related to EGFR, mTORC1, and EMT were upregulated in the high *EREG* expression group (highest 40 cases of *EREG* expression) in comparison with those in the low *EREG* expression group (lowest 40 cases). NES, nominal p value, and FDR are shown in each plot. (D) Representative images of IHC for ELF3, EREG, p-EGFR, and p-4E-BP1 in intraepithelial/submucosal and invasive portions of human GBC; the graphs show the IHC staining intensity for ELF3, EREG, p-EGFR, and p-4E-BP1 between intraepithelial and invasive portions in human GBC tissues (n = 47). Insets show higher-magnification images. Scale bars, 100 μm. Means ± SEM. $^{**}p < 0.01$, $^{****}p < 0.0001$, Paired t-test.

Supplementary Tables

Supplementary Tables S1 provided as a separate Excel file

Table S2. Antibodies for IHC, western blotting, and ChIP assay used in this study.

Antibodies	Supplier	Catalogue No.	Dilution
Mouse ELF3 (IHC, ChIP)	Invitrogen*	PA5-47776	1:300 (IHC) 1:500 (ChIP)
Human ELF3 (IHC)	Sigma-Aldrich	HPA003479	1:200
E cadherin (IHC, WB)	Cell Signaling Technology	3195	1:200 (IHC) 1:1000 (WB)
N cadherin (IHC, WB)	Cell Signaling Technology	13116	1:100 (IHC) 1:1000 (WB)
ZEB1 (IHC, WB)	Sigma-Aldrich	HPA027524	1:1000 (IHC) 1:2500 (WB)
Mouse EREG (IHC)	Santa Cruz†	sc-376284	1:50
Human EREG (IHC)	R&D systems‡	AF1195	1:100
EGFR (WB)	Cell Signaling Technology	4267	1:1000
Phospho-EGFR (Try1068) (D7A5) (WB)	Cell Signaling Technology	3777	1:1000
Phospho-EGFR (Try1068) (IHC)	Abcam§	ab40815	1:200
PI3K p85 (WB)	Cell Signaling Technology	4257	1:500
Phospho-PI3K p85 (Tyr458)/p55 (Tyr199) (WB)	Cell Signaling Technology	4228	1:500
AKT (WB)	Cell Signaling Technology	4691	1:1000
Phospho-AKT (ser473) (WB)	Cell Signaling Technology	4060	1:2000

Phospho-RPS6 (ser235/236) (D57.2.2E) (IHC)	Cell Signaling Technology	4858	1:200
RPS6K (WB)	Cell Signaling Technology	2708	1:1000
Phospho-RPS6K (Thr389) (WB)	Cell Signaling Technology	9205	1:1000
4E-BP1 (WB)	Cell Signaling Technology	9644	1:1000
Phospho-4E-BP1 (IHC, WB)	Cell Signaling Technology	2855	1:1000 (IHC) 1:1000 (WB)
p44/42 MAPK 1/2 (WB)	Cell Signaling Technology	9102	1:1000
Phospho-p44/42 MAPK 1/2 (Thr202/Tyr204) (IHC, WB)	Cell Signaling Technology	4370	1:300 (IHC) 1:2000 (WB)
AMPKα (WB)	Cell Signaling Technology	2532	1:1000
Phospho-AMPKα (Thr172) (40H9) (WB)	Cell Signaling Technology	2535	1:1000
SNAI1 (WB)	Proteintech¶	13099-1-AP	1:500
β-actin (WB)	Abcam	ab6276	1:5000
Mouse IgG HRP Linked Whole Ab (WB)	Cytiva**	NA931	1:4000
Donkey anti-rabbit IgG (H+L) Cross-Absorbed, HRP (WB)	Thermo Fisher Scientific	31458	1:10000

WB, western blotting.

* Invitrogen, Waltham, MA, USA.

† Santa Cruz Biotechnology, Dallas, TX, USA.

‡ R&D systems, Minneapolis, MN, USA

§ Abcam, Cambridge, UK

¶ Proteintech, Rosemont, IL, USA

** Cytiva, Tokyo, Japan

Table S3. Primer sets for RT-qPCR, ChIP, and genotyping used in this study.

Gene symbols	Forward	Reverse
RT-qPCR		
Elf3	TCCTCCGACTACCTTTGGCA	ATCAGTCCTGTCCCTTTGGG
Ereg	CTGCCTCTTGGGTCTTGACG	GCGGTACAGTTATCCTCGGATTC
Areg	GGTCTTAGGCTCAGGCCATTA	CGCTTATGGTGGAAACCTCTC
Gapdh	AGGTCGGTGTGAACGGATTTG	TGTAGACCATGTAGTTGAGGTCA
Cdh1	AAAAGAAGGDTGTCCTTGGC	GAGGTCTACACCTTCCCGGT
Cdh2	CAGGGTGGACGTCATTGTAG	AGGGTCTCCACCACTGATTC
Zeb1	GCTGGCAAGACAACGTGAAAG	GCCTCAGGATAAATGACGGC
Snai1	CACACGCTGCCTTGTGTCT	GGTCAGCAAAAGCACGGTT
Cd133	ACTGGGGCTGTGTGGAAAG	GCATTGAAGGTATCTTGGGTCTC
Sox17	GATGCGGGATACGCCAGTG	CCACCTCGCCTTTCACCTTTA
Slc28a3	GACCTTGAACGGCAGAACACT	CTTTGTTTCCTAGAGGCTCCTG
Kcne3	ATGGAGACTTCCAACGGGACT	CCGGCAGAGCAAGTGACTG
ChIP		
Ereg **promoter**	AGAGCAAACCAACCCATCTG	CTAGGCACGCGAGGACTTAC
Areg **promoter**	GGAGTCCTTTAGCGCTTCGT	TACGCGGGGAGAAACTTTCC
Genotyping		
$Kras^{G12D}$	ATGTCTTTCCCCAGCACAGT	TCCGAATTCAGTGACTACAGATG
$Trp53^{R172H}$	GCCTTGCACCTTTCCAACTG	CTTGGAGACATAGCCACACTG

ELF3 suppresses gallbladder cancer development through downregulation of the EREG/EGFR/mTOR complex 1 signalling pathway
T Nakamura *et al. J Pathol* DOI: 10.1002/path.6144

Table S1. Clinical information of 85 patients with GBC

Supplementary Table S1. Clinical information of 85 patients with GBC.

Sample	Age	Sex	Stage	T Stage	N stage	M stage	Main histological type	ELF3 staining intensity	Initial treatment	Evaluated tissue	Recurrence after resection	Interval to death or censored	Death or censored
1	68	F	0	Is	0	0	tub1	0	Surgery	Primary lesion	No	1,642	Death
2	72	F	IIA	2	0	0	tub1	0	Surgery	Primary lesion	Yes	1,371	Death
3	80	F	IIB	2	0	0	pap	0	Surgery	Primary lesion	No	5,403	Censored
4	61	F	IIIA	3a	0	0	adsq	0	Surgery	Primary lesion	Yes	162	Death
5	63	M	IIIA	3a	0	0	asc	0	Surgery	Primary lesion	Yes	495	Death
6	73	M	IIIA	3a	0	0	tub2-por	0	Surgery	Primary lesion	Yes	98	Death
7	77	M	IVB	4a	0	1	NA	0	BSC	Metastatic lesion	-	9	Censored
8	81	F	IIIB	3a	1	0	tub2-por	0	Surgery	Primary lesion	No	1,084	Death
9	63	F	IVB	4b	1	1	NA	0	Chemotherapy	Metastatic lesion	-	82	Death
10	70	M	IVB	3	1	1	tub2	0	Surgery	Primary lesion	Yes	205	Death
11	81	M	IVB	3a	1	1	undiff	0	Surgery	Primary lesion	Yes	50	Death
12	71	F	IB	1b	0	0	tub1	0	Surgery	Primary lesion	No	1,531	Censored
13	70	M	IVB	3b	1	1	tub1	0	Surgery	Primary lesion	No	391	Censored
14	54	M	0	Is	0	0	tub1	1	Surgery	Primary lesion	No	1,826	Censored
15	66	M	0	Is	0	0	tub1	1	Surgery	Primary lesion	No	10	Censored
16	81	M	0	Is	0	0	tub1	1	Surgery	Primary lesion	No	1,206	Censored
17	59	M	0	Is	0	0	tub1	1	Surgery	Primary lesion	No	4,959	Censored
18	88	M	IB	1b	0	0	tub1	1	Surgery	Primary lesion	No	147	Censored
19	65	M	IIA	2	0	0	MANEC	1	Surgery	Primary lesion	No	2,036	Censored
20	66	M	IIB	2	0	0	tub2	1	Surgery	Primary lesion	No	2,508	Censored
21	74	F	IIB	2	0	0	tub1	1	Surgery	Primary lesion	No	3,576	Death
22	79	M	IIB	2	0	0	tub1>pap	1	Surgery	Primary lesion	No	1,692	Censored
23	55	F	IIIA	3	0	0	pap, tub1, tub3	1	Surgery	Primary lesion	No	4,209	Censored
24	67	M	IIIA	3a	0	0	tub2	1	Surgery	Primary lesion	Yes	2,047	Censored
25	80	F	IIIA	3b	0	0	tub2	1	Surgery	Primary lesion	No	1,819	Censored
26	74	F	IIIA	3b	0	0	tub2>por2	1	Surgery	Primary lesion	Yes	642	Death
27	44	M	IIIB	3a	1	0	pap>tub1	1	Surgery	Primary lesion	Yes	619	Death
28	59	F	IIIB	3a	1	0	tub2>pap>por1	1	Surgery	Primary lesion	Yes	421	Death
29	61	F	IIIB	2	1	0	pap>tub2	1	Surgery	Primary lesion	Yes	462	Death
30	71	F	IIIB	3b	1	0	tub2	1	Surgery	Primary lesion	Yes	1,160	Death
31	76	F	IIIB	2	1	0	tub2	1	Surgery	Primary lesion	No	1,162	Censored
32	85	F	IIIB	3a	1	0	cs	1	Surgery	Primary lesion	Yes	228	Death
33	59	F	IVA	4b	1	0	tub2>1, por	1	Surgery	Primary lesion	Yes	466	Death
34	54	M	IVB	3a	1	1	por	1	Chemotherapy	Metastatic lesion	-	160	Death
35	61	F	IVB	4a	1	1	tub3	1	Surgery	Primary lesion	Yes	482	Death
36	68	F	IVB	3a	1	1	tub2+undiff	1	Surgery	Primary lesion	Yes	120	Death
37	68	M	IVB	3a	1	1	adenocarcinoma	1	Chemotherapy	Metastatic lesion	-	576	Death
38	70	M	IVB	3a	1	1	adenocarcinoma	1	Chemotherapy	Metastatic lesion	-	313	Death
39	72	F	IVB	3b	1	1	tub2	1	Surgery	Primary lesion	Yes	393	Death
40	74	M	IVB	3a	1	1	NA	1	Surgery	Primary lesion	No	762	Death
41	56	M	IVB	3a	2	1	tub2>por	1	Surgery	Primary lesion	Yes	41	Death
42	61	M	IVA	4a	1	0	por-undiff	1	Surgery	Primary lesion	Yes	14	Death
43	59	M	0	is	0	0	tub1	1	Surgery	Primary lesion	No	388	Censored
44	72	M	IIA	2	0	0	tub1	1	Surgery	Primary lesion	No	1,167	Censored
45	64	M	IVB	3a	1	1	tub2>pap	1	Surgery	Primary lesion	Yes	332	Death

46	78	F	0	is	0	0	pap	2	Surgery	Primary lesion	No	3,200	Death
47	67	F	I	1b	0	0	tub2	2	Surgery	Primary lesion	No	1,428	Censored
48	68	M	IA	1a	0	0	tub1	2	Surgery	Primary lesion	No	3,580	Censored
49	77	F	IB	1b	0	0	tub1	2	Surgery	Primary lesion	No	5,804	Censored
50	79	M	IB	1b	0	0	tub1	2	Surgery	Primary lesion	No	1,852	Censored
51	65	M	IIA	2	0	0	tub1	2	Surgery	Primary lesion	No	1,112	Censored
52	77	F	IIA	2	0	0	tub1>pap	2	Surgery	Primary lesion	No	4,521	Censored
53	53	F	IIB	2	0	0	tub1	2	Surgery	Primary lesion	No	4,684	Censored
54	67	F	IIB	2	0	0	pap, tub1	2	Surgery	Primary lesion	Yes	1,324	Death
55	72	F	IIB	2b	0	0	tub2	2	Surgery	Primary lesion	No	5,976	Death
56	78	M	IIB	2	0	0	tub1	2	Surgery	Primary lesion	No	3,660	Death
57	78	M	IIB	2	0	0	tub1-2	2	Surgery	Primary lesion	No	2,708	Censored
58	82	F	IIB	2	0	0	tub1-2	2	Surgery	Primary lesion	No	1,444	Death
59	79	F	IIIA	3a	0	0	tub2	2	Surgery	Primary lesion	Yes	1,713	Death
60	62	F	IVB	4a	0	1	tub2	2	Chemotherapy	Metastatic lesion	-	212	Death
61	79	M	IIIB	2	1	0	tub2	2	Surgery	Primary lesion	Yes	326	Death
62	55	M	IVB	3a	1	1	scc	2	Chemotherapy	Metastatic lesion	-	63	Death
63	57	M	IVB	4b	1	1	tub2-por	2	Chemotherapy	Metastatic lesion	-	157	Death
64	65	F	IVB	3a	1	1	tub1	2	Chemotherapy	Metastatic lesion	-	799	Death
65	71	F	IVB	2	1	1	tub3	2	Surgery	Primary lesion	Yes	350	Death
66	74	M	IVB	4a	1	1	tub2	2	Surgery	Primary lesion	Yes	702	Death
67	77	F	IVB	3a	1	1	adenocarcinoma	2	Chemotherapy	Metastatic lesion	-	371	Death
68	83	F	IVB	3	2	1	tub2	2	Surgery	Primary lesion	Yes	240	Death
69	43	M	0	is	0	0	tub1	2	Surgery	Primary lesion	No	540	Censored
70	84	F	IIB	2	0	0	tub2, por	2	Surgery	Primary lesion	No	3,334	Death
71	85	F	IIB	2	0	0	tub2	2	Surgery	Primary lesion	Yes	566	Death
72	72	M	0	is	0	0	Pap	3	Surgery	Primary lesion	No	391	Censored
73	49	F	IA	1a	0	0	pap, tub1	3	Surgery	Primary lesion	No	4,034	Censored
74	78	F	IB	1b	0	0	pap>tub1	3	Surgery	Primary lesion	Yes	827	Censored
75	65	F	IIA	2	0	0	tub2	3	Surgery	Primary lesion	No	357	Censored
76	66	M	IIB	2	0	0	pap>tub1>por2	3	Surgery	Primary lesion	No	538	Censored
77	78	M	IIB	2	0	0	tub1	3	Surgery	Primary lesion	No	648	Censored
78	73	F	IIIA	3a	0	0	tub2	3	Surgery	Primary lesion	No	5,211	Censored
79	68	F	IVB	4a	0	1	adenocarcinoma	3	Chemotherapy	Metastatic lesion	-	572	Death
80	72	F	IIIB	2	1	0	tub1, pap	3	Surgery	Primary lesion	Yes	408	Death
81	60	F	IVB	3	1	1	tub2>tub3>pap	3	Surgery	Primary lesion	Yes	1,222	Death
82	75	M	IVB	4a	1	1	adenocarcinoma	3	Chemotherapy	Metastatic lesion	-	111	Death
83	88	F	0	is	0	0	pap	3	Surgery	Primary lesion	No	471	Death
84	73	F	IIA	2	0	0	pap>tub2	3	Surgery	Primary lesion	No	906	Censored
85	63	M	IIIB	3a	1	0	tub1	3	Surgery	Metastatic lesion	No	4,441	Censored

BSC, best supportive care; NA, Not available.